UNIWERSYTET JAGIELLOŃSKI
WYDZIAŁ FIZYKI, ASTRONOMII
I INFORMATYKI STOSOWANEJ
INSTYTUT FIZYKI im. MARIANA SMOLUCHOWSKIEGO

Studia porównawcze oddziaływania w niskoenergetycznych układach $pp\eta$ i $pp\eta'$

Paweł Klaja

praca przygotowana w Zakładzie Fizyki Jądrowej
Instytutu Fizyki im. Mariana Smoluchowskiego,
Wydziału Fizyki, Astronomii i Informatyki Stosowanej Uniwersytetu Jagiellońskiego, oraz
w Instytucie Fizyki Jądrowej w Centrum Badawczym Jülich,
pod kierunkiem Prof. Pawła Moskala.

Kraków 2009

JAGIELLONIAN UNIVERSITY
FACULTY OF PHYSICS, ASTRONOMY
AND APPLIED COMPUTER SCIENCE
MARIAN SMOLUCHOWSKI INSTITUTE OF PHYSICS

Comparative studies of the interaction in the low energy $pp\eta$ and $pp\eta'$ systems

Paweł Klaja

dissertation prepared at the Nuclear Physics Department
of the Marian Smoluchowski Institute of Physics, at Faculty of Physics, Astronomy and Applied
Computer Science of the Jagiellonian University
and in Institute of Nuclear Physics at Research Centre Jülich,
guided by Prof. Paweł Moskal.

Cracow 2009

"To są kulki proszę Państwa, na 100%."

P. M.

Abstract

The COSY-11 collaboration measured the $pp \rightarrow pp\eta$ and $pp \rightarrow pp\eta'$ reactions in order to perform comparative studies of the interactions within the proton-proton-meson system.
This thesis presents in detail the analysis of the $pp \rightarrow pp\eta'$ reaction which was measured at the proton beam momentum of 3.260 GeV/c.
The elaboration results in differential distributions of squared invariant proton-proton (s_{pp}) and proton-η' ($s_{p\eta'}$) masses, as well as in angular distributions and the total cross section at an excess energy of 16.4 MeV.
The differential distributions s_{pp} and $s_{p\eta'}$ are compared to theoretical predictions and to the analogous spectra determined for the $pp \rightarrow pp\eta$ reaction.
The comparison of the results for the η and η' meson production rather excludes the hypothesis that the enhancement observed in the invariant mass distributions is due to the meson-proton interaction.
Further, the shapes of the distributions do not favour any of the postulated theoretical models.

Streszczenie

W ramach grupy badawczej COSY-11 wykonano pomiary reakcji $pp \rightarrow pp\eta$ oraz $pp \rightarrow pp\eta'$ w celu przeprowadzenia studiów porównawczych oddziaływania w układzie proton-proton-mezon.
W rozprawie doktorskiej zaprezentowano analizę danych z pomiaru reakcji $pp \rightarrow pp\eta'$ wykonanego z wykorzystaniem wiązki protonowej o pędzie 3.260 GeV/c.
Wynikiem analizy przedstawionej w niniejszej pracy są różniczkowe przekroje czynne w funkcji mas niezmienniczych proton-proton (s_{pp}) i proton-η' ($s_{p\eta'}$), rozkłady kątowe oraz całkowity przekrój czynny dla energii wzbudzenia Q = 16.4 MeV.
Rozkłady różniczkowe s_{pp} oraz $s_{p\eta'}$ zostały porównane z przewidywaniami teoretycznymi oraz analogicznymi widmami otrzymanymi dla reakcji $pp \rightarrow pp\eta$.
Porównanie rezultatów otrzymanych dla produkcji mezonów η i η' pozwala na wykluczenie hipotezy, że wzmocnienie obserwowane w widmach mas niezmienniczych jest powodowane oddziaływaniem mezonu z protonem.
Co więcej, na podstawie kształtu otrzymanych dystrybucji nie da się rozstrzygnąć pomiędzy poprawnością założeń w postulowanych modelach teoretycznych.

Contents

1. Introduction

The knowledge of the meson-nucleon interaction at the hadronic level is one of the major goals in nuclear physics, nowadays. Also, studies of meson structure and production mechanisms constitute a huge interest of nuclear and particle physicists. During the last decades many measurements produced interesting results [1], but various questions are still open.

In the SU(3)-flavour scheme the η and η' mesons belong to the nonet meson family of pseudoscalar mesons. The η and η' mesons constitute a mixture of states: singlet-η_1 and octet-η_8.

It is important to stress that the strength of the $p\eta$ and $p\eta'$ interaction depends on the structure of the η and η' mesons and is directly related to the singlet-η_1 and octet-η_8 contributions in the wave functions of these mesons [2–4].

Taking into account the mixing angle the resulting contribution of the various quark flavours in the η and η' wave function is almost the same. However, in spite of the postulated similar quark structure the η and η' mesons owe unexpectedly different features.

The most drastic ones are:

- η and η' mesons possess different masses, the $\eta(547)$ meson is almost two times lighter than the $\eta'(958)$ meson [5].
- The branching ratios of B and D_s mesons for the decays into the η' meson are higher than for the decays into the η meson, and deviate strongly from model predictions [6, 7].
- There is no experimental evidence for baryonic resonance which decays by the emission of an η' meson [5, 8] while e.g. the resonances N(1535) and N(1650) decay via the emission of the η meson with a significant probability [5].

These different features could imply a possible difference in the interaction of η and η' mesons with elementary particles, and indicate that also the production mechanism of both mesons in elementary particle collisions might vary.

Due to the short life-time of the flavour neutral pseudoscalar mesons, experiments with meson beams or targets are difficult or hardly feasible. Therefore, the nucleon-meson interaction can be studied only via its influence on the cross sections of the reactions during which they are produced (e.g. $NN \rightarrow NN\ Meson$) [1].

Quantitative information about the interaction can be gained from the shape of the excitation functions for the $pp \rightarrow pp\eta$ and $pp \rightarrow pp\eta'$ reactions as well as from a comparison of those to the $pp\pi^0$ system.

Up to now, only the proton interaction with pions and the η-meson [1] was studied more exhaustively due to much more higher total cross sections in comparison to the cross section for the $pp \to pp\eta'$ reaction.
Besides the excitation function also differential distributions of invariant proton-proton and proton-meson masses constitute a sensitive tool for studies of the interaction within the meson-nucleon system. The distribution of the proton-η invariant mass showed a clear enhancement in the region of small proton-η relative momenta [9]. The observed effect could be explained by the non negligible role of the proton-η interaction in the final state [10, 11], the admixture of higher partial waves during the η production [12], or the energy dependence of the production amplitude [13]. Using only the $pp \to pp\eta$ data, it is however not possible to justify or falsify any of the above mentioned hypothesis.

The endeavour to explain the observed enhancement motivated the experiment and the analysis of the $pp \to pp\eta'$ reaction which is presented in this thesis. This experiment was performed using the COSY-11 detector setup [14–16], installed at the cooler synchrotron COSY [17] at the Research Centre Jülich in Germany. It was conducted in an energy range close to the kinematical threshold for the η' meson production, where the relative velocities of the produced particles are small.
The analysis and results of the $pp \to pp\eta'$ reaction measurement, conducted in order to determine the distribution of events over the phase space for an excess energy range equal to the one measured before for the $pp \to pp\eta$ reaction are presented in this thesis. The measurement was performed at the nominal beam momentum of 3.257 GeV/c corresponding to the nominal excess energy for the $pp\eta'$ reaction equal to 15.5 MeV. The analysis of the $pp\eta'$ data was performed in a similar way as it has been done for the $pp\eta$ system.
The comparison of the differential distributions for the proton-proton and for the proton-meson invariant masses in the η and η' production could help to judge about the validity of postulated theories concerning the observed enhancement and allows for a quantitative estimation of the relative strength of the proton-η and the proton-η' interactions, provided that the effect is caused by the proton-meson interaction.

In the following chapter the current status of the $pp \to pp\eta$ and $pp \to pp\eta'$ total cross section measurements is presented. Furthermore, the possibility of proton-η and proton-η' interaction studies is discussed and the description of the observables used in the analysis described in this thesis is given. The results achieved for the $pp \to pp\eta$ measurement as well as the available theoretical descriptions of the results are presented.
Chapter 3 is devoted to the presentation of the experimental facility used to perform the $pp \to pp\eta'$ measurement. In the next chapter, the methods used for the calibration of the COSY-11 detectors and their relative geometrical settings are presented. The time-space relation of the drift chambers and the procedure for the time-of-flight calibration is described. Also, the procedure used for the monitoring of the relative beam-target setting is discussed.

In chapter 5 the method of the $pp \to pp\eta'$ reaction identification will be depicted and the method of identifying measured and also unobserved particles will be given.
Further on, the procedure of the luminosity (L) determination will be presented in chapter 6, and in the consecutive chapters it will be shown how the absolute value and the spread of the beam momentum was extracted, and the method for the determination of the position of the drift chambers relative to the COSY-11 dipole will be explained.
Chapter 9 comprises the evaluation procedure of the differential distributions. First, the kinematical fit procedure and then the background subtraction due to the multi-pion production will be discussed.
The final results concerning the total cross section and differential distributions are presented in chapter 10. The acceptance corrections are discussed and the achieved experimental results are compared to theoretical predictions.
The conclusions are presented in chapter 11.
In the appendices at the end of the dissertation some issues discussed in the thesis are explained in more detail. In the first one the structure of the pseudoscalar meson nonet, meson masses and quark structure are presented. The second one is devoted to the description of the parameterization of the on-shell proton-proton interaction. General remarks about the combined analysis of the η' meson formalism in photo- and hadro-production are presented in the third addendum, and the linear energy dependence of the production amplitude is discussed in the last one.

2. Low energy interaction within a proton-proton-meson system

The interaction of hadrons is the reflection of the strong force between the quarks, and provides information about the hadron structure and the strong interaction itself [1]. In the framework of the optical model, the interaction between hadrons can be expressed in terms of phase-shifts, which in the zero energy limit are described by the scattering length and effective range parameters [1]. These variables are quite well established for the (low-energy) nucleon-nucleon interaction [18, 19], but they are poorly known for the nucleon-meson or meson-meson interactions. The estimated real part of the scattering length of the η-proton potential, depending on the method of the analysis and studied region, is 3 to 10 times [1] larger than for the π^0-proton scattering ($a_{p\pi^0} = 0.13$ fm) [20,21], while for the η' meson only an upper limit is known of 0.8 fm [22].
The interaction of mesons (e.g. pseudoscalar mesons[1]: π, K, η, η') with nucleons could be deduced from the experiments realized by means of meson beams, but such experiments are not feasible in case of the flavour neutral mesons due to their short lifetime [1,5]. However, the study of their interaction with hadrons is certainly accessible via their influence on the cross section of reactions like $NN \to NN\ Meson$ in which they are produced [1]. In such a case, the interaction within the final meson–nucleon system will modify the shape of the excitation function and of the differential distributions of invariant masses of the nucleon-nucleon-meson systems.

2.1 Excitation functions for $pp \to pp\eta$ and $pp \to pp\eta'$ reactions

Near the kinematical threshold measurements of nucleon-nucleon collisions allow to study the particle production with a dominant contribution from one partial wave only. In this energy range, the dependence of the total cross section as a function of the centre-of-mass excess energy is predominantly determined by the available phase space and the interaction between the exit particles. The excitation functions for the $pp \to pp\eta'$ [23–28] and $pp \to pp\eta$ [28–33] reactions are presented in figure 2.1. Comparing the data to the arbitrarily normalized phase-space integral reveals that proton-proton FSI enhances the total cross section by more than one order of magnitude for low energies. In case of the η' meson production one recognizes that the data are described well assuming that the on-shell proton-proton amplitude exclusively determines the phase-space population.

[1] The features of the pseudoscalar meson nonet are described in appendix A.

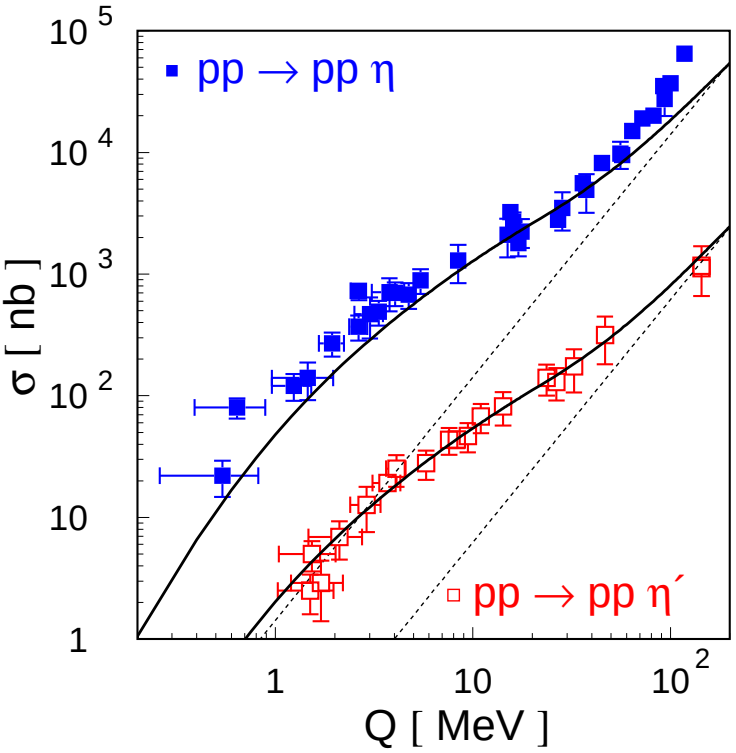

Figure 2.1: The $pp \to pp\eta$ and $pp \to pp\eta'$ excitation functions [23–33]. The dashed lines indicate arbitrarily normalized functions obtained under the assumption of the homogeneous phase space occupation. Solid lines correspond to calculations of the phase space weighted by the proton-proton on-shell scattering amplitude [22].

This indicates that the proton-η' interaction is too small to manifest itself in the excitation function within the presently achieved statistical uncertainty. However, for the η meson production the enhancement is by about a factor of two larger than in case of the η' meson and cannot be described by the pp-FSI only.

2.2 Comparison of η, η' and π^0 meson interaction with protons

The strength of the interaction deduced from the comparison of the data and the lines in figure 2.1 depends on the model of the proton-proton interaction used in the calculations for the $pp\eta$ and $pp\eta'$ systems [22]. Therefore, in order to estimate a relative strength between the $p\eta$ and $p\eta'$ interactions in a model independent way one can compare the shape of the excitation function of the $pp \to pp\eta$ and $pp \to pp\eta'$ reactions. Moreover, one can gain some quantitative information about these interactions by a comparison of these shapes to the $pp\pi^0$ system [1], since the π^0-proton scattering length is well known and amounts to 0.13 fm [20, 21].

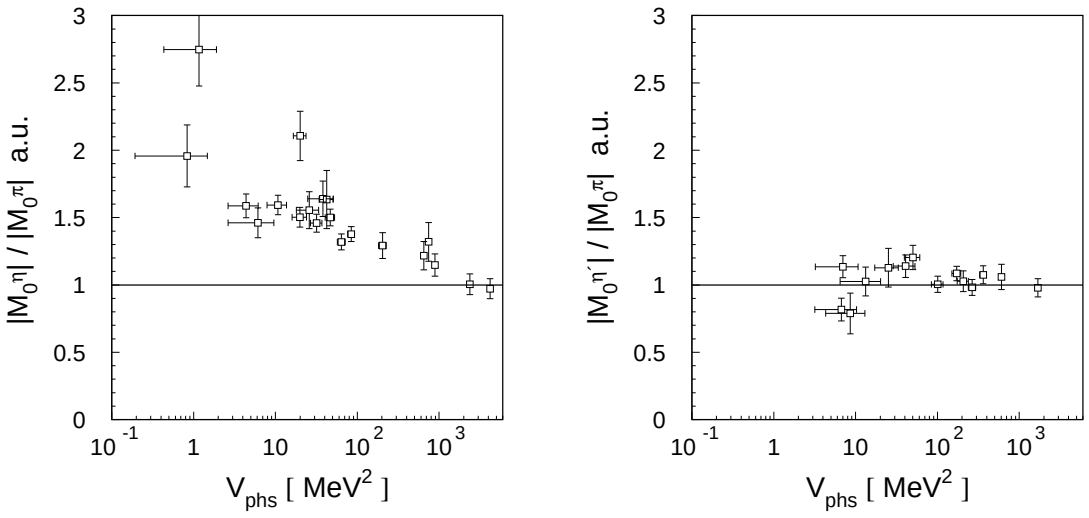

Figure 2.2: The ratios $|M_0^{\eta}|/|M_0^{\pi}|$ (left) and $|M_0^{\eta'}|/|M_0^{\pi}|$ (right) extracted from data calculating the *pp*-FSI according to the formulas from reference [22], and neglecting the proton-meson interaction [1]. The ratio is shown as a function of the phase space volume [22].

For that purpose, one can compare only the dependence of the production amplitudes $|M_0|$ derived from the data taking into account the *pp*-FSI only.
The dependence of $|M_0^{\eta}|$ and $|M_0^{\eta'}|$ as a function of the phase space volumes normalized to $|M_0^{\pi}|$ are presented in figure 2.2. The $|M_0|$ for the η, η' and π^0 mesons were extracted from data, disregarding any proton-meson interaction. When the neglected $\eta(\eta')$-proton interaction would have been the same as the one for proton-π^0, the points in the plots should have been consitent with unity as can be seen for the $pp \to pp\eta'$ reaction, when really the interaction shows its weakness, independently of the prescription used for the proton-proton final state interaction [22]. In the case of the η' meson production its weak interaction with nucleons at the low-energy range is expected due to the lack of any baryonic resonances which could decay into a $N\eta'$ system [1,8][2].

Statistical uncertainties allowed to get only a very conservative upper limit for the real part of the scattering length of the proton-η' potential resulting in:
$|Re\ a_{p\eta'}| \ < \ 0.8\ fm$ [1,26].
Thus, independent of the model used for the prescription of the *pp*-FSI, from a comparison of the energy dependence of the production amplitudes for the $pp \to pp\eta$, $pp \to pp\eta'$ and $pp \to pp\pi^0$ reactions, it was concluded that the interaction within the proton-η' system is much weaker than the interaction between the proton and the η meson.
Another possibility of learning about interactions within nucleon-nucleon-meson systems

[2]Recent calculations of K. Nakayama, Y. Oh and H. Haberzettl predict also resonance state contributions for the photo- and hadro-productions [34].

is given by the differential distributions of the invariant masses. This is why the present analysis of the $pp\eta'$ system has been performed in a similar way as it has been done earlier [9] for the $pp\eta$ system. The determined pp and p-meson invariant mass distributions will be used for a comparative study of the interaction within the proton-meson system.
In the next section the definitions of the studied observables which will be used in the further analysis are presented.

2.3 Definitions of observables

To describe the studied three particle ($pp\eta'$) system one needs only five independent variables in the centre-of-mass system. In this frame, due to energy and momentum conservation, momentum vectors of protons and η' lie in one plane, called reaction plane. In that plane (shown schematically in figure 2.3) the relative momenta of particles are described by only two variables. These quantities may be chosen as square of the proton-proton invariant mass s_{pp} and square of the proton-η' invariant mass $s_{p\eta'}$. Invariant masses depend on the relative velocity of the particles and are therefore well suited for a description of the interactions between these particles. Besides the relative movement of particles on the reaction plane three other variables have to be defined for fixing the orientation of the reaction plane in the coordinate system.

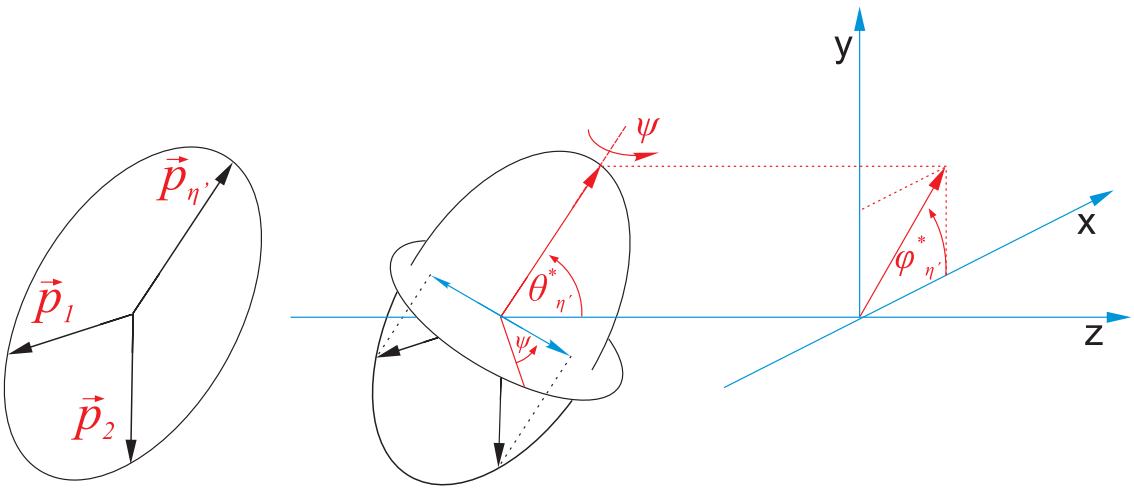

Figure 2.3: Schematic definitions of the centre-of-mass kinematical variables used for the description of the $pp\eta'$ system. In the centre-of-mass frame the momentum vectors of the three outgoing particles are located within the reaction plane. In this plane the relative motion of the ejectiles is fixed by the square of the invariant masses s_{pp} and $s_{p\eta'}$. Three remaining variables the $\phi^*_{\eta'}$, $\theta^*_{\eta'}$ and ψ angles are used to define the orientation of the emission plane in space.

In this thesis, by analogy to the evaluation of the $pp\eta$ system [9], the azimuthal and polar angles of the η' meson momentum vector relative to the beam direction, denoted as $\phi^*_{\eta'}$ and $\theta^*_{\eta'}$ are used, respectively, and the ψ angle describing the rotation of the reaction plane

around the direction of the momentum vector of the η' meson.
The interaction between final state particles does not alter the orientation of the reaction plane [9]. Therefore, it will manifest itself only in the distribution of the invariant masses s_{pp} or $s_{p\eta'}$, or generally in the population of the Dalitz plot (s_{pp} vs. $s_{p\eta'}$).
In the case of non-interacting particles in the final state these distributions should correspond to a homogeneously populated phase space. Therefore, their interaction should show up as a deviation from these expectation.

2.4 pp and $p-meson$ invariant mass distributions

Only two invariant masses of three subsystems are independent and therefore the whole accessible information about the final state interaction can be shown in the Dalitz plot. One can also use the projection of the phase-space distribution onto the invariant masses of proton-proton or proton-meson subsystems [9].

The qualitative phenomenological analysis of the determined differential invariant proton-proton and proton-η mass distributions revealed an enhancement of the population density at the kinematical region corresponding to a small proton-η momentum. The proton-proton and proton-η invariant mass distributions determined for the $pp \to pp\eta$ reaction at an excess energy of 15.5 MeV are presented in figure 2.4[3]. The dashed lines in both panels of the figure depict the results of calculations where only the on-shell amplitude of the proton-proton interaction has been taken into account.

In those calculations the enhancement factor has been estimated as the square of the on-shell proton-proton scattering amplitude derived using the modified Cini-Fubini-Stanghellini formula including the Wong-Noyes Coulomb corrections [22].
One can easily see that the mentioned effect is too large to be described by the on-shell inclusion of the proton-proton FSI.

In fact a better description is achieved when contributions from higher partial waves or off-shell effects of the proton-proton potential are taken into account. These calculations compared to the experimentally determined differential proton-proton invariant mass distribution are presented in figure 2.5. In the left panel of this figure the experimentally determined differential cross section as a function of the squared invariant proton-proton mass is compared to the calculations of V. Baru and collaborators [39] under the assumption of a ${}^3P_0 \to {}^1S_0 s$ transition according to the models described in [39], depicted as the solid line.
Dashed and dotted lines on the left panel of figure 2.5 represent the calculations of K. Nakayama and his group [12]. The authors claim that the contribution of the S-wave alone is unable to explain the observed enhancement in the squared proton-proton invariant

[3] A similar enhancement has been observed for several measurements performed at excess energies of 4.5 MeV [9], 10 MeV [35, 36], 15 and 41 MeV [37], and 72 MeV [38].

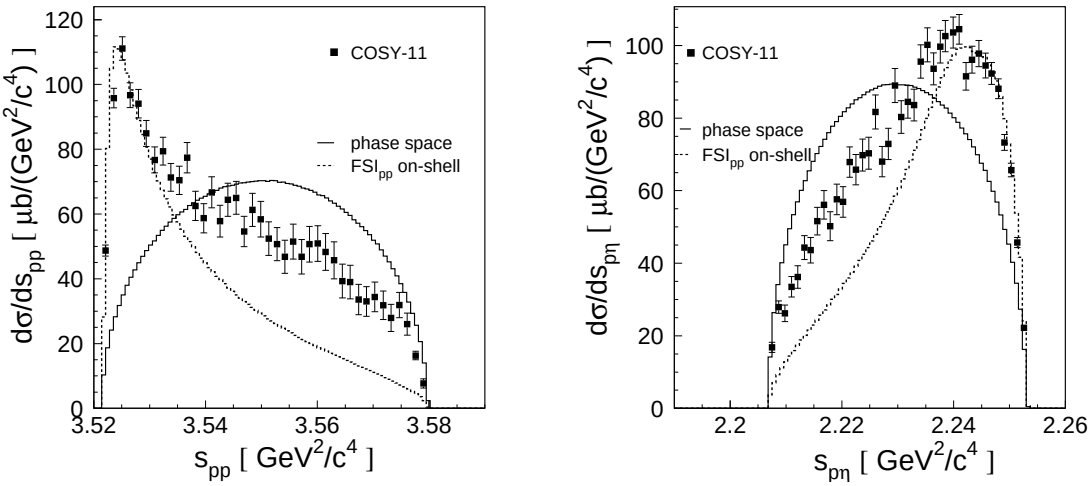

Figure 2.4: Distributions of the square of the proton-proton (s_{pp}) (left) and proton-η ($s_{p\eta}$) (right) invariant masses determined experimentally for the $pp \to pp\eta$ reaction (closed squares). The integrals of the phase space weighted by the square of the proton-proton on-shell scattering amplitude (dotted lines)-FSI$_{pp}$ have been normalized arbitrarily at small values of s_{pp}. The expectations under the assumption of a homogeneously populated phase space are shown as solid lines.

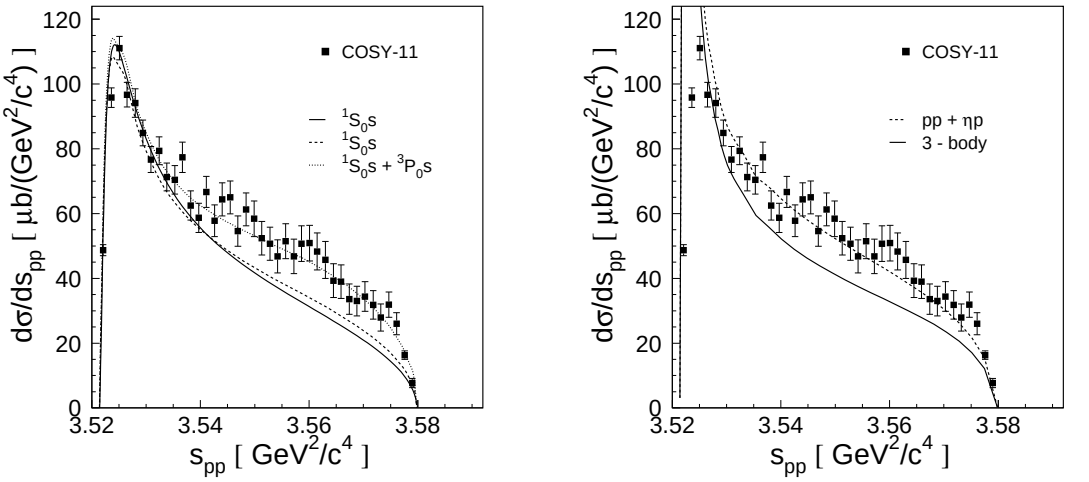

Figure 2.5: (Left panel) Distribution of the square of the proton-proton (s_{pp}) invariant mass determined experimentally for the $pp \to pp\eta$ reaction. Solid and dashed lines correspond to calculations under the assumption of a $^3P_0 \to ^1S_0 s$ transition according to the models described in [39] and [12], respectively. The dotted line shows the result of calculations with inclusion of the $^1S_0 \to ^3P_0 s$ contribution as suggested in [12]. (Right panel) The same data as in the left panel but compared with three-body calculations [10,11]. The solid line was determined with a rigorous three-body approach. The dashed line depicts the situation if only pairwise interactions ($pp + p\eta$) are allowed.

mass distribution. Seeking for the better description they postulate that the shape of the enhancement can be reproduced by folding the relative momentum of the proton-proton subsystem with the available phase space [12] suggesting that the enhancement could be the consequence of the *pp* P-wave in the final state.
Calculations assuming a ${}^3P_0 \rightarrow {}^1S_0 s$ transition correspond to the dashed curve and the result of calculations with the inclusion of the ${}^1S_0 \rightarrow {}^3P_0 s$ contribution is depicted by the dotted line. Although the dotted line corresponding to calculations based on the stronger P-wave contribution is in quite good agreement to the experimental determined differential distribution of the proton-proton invariant mass, it underestimates the total cross section data taken for the $pp \rightarrow pp\eta$ reaction near the kinematical threshold (Q lower than 30 MeV) [1].

On the other hand, the discussed effect can in principle be assigned to changes of the production amplitude, since in calculations by V. Baru et al. [39], and by K. Nakayama and collaborators [12] the production amplitude was nearly constant.
An analysis guided by the assumption of a linear energy dependence of the production amplitude was performed by A. Deloff [13]. The squared invariant mass distributions s_{pp} and $s_{p\eta}$ determined for the $pp \rightarrow pp\eta$ reaction measured at an excess energy of Q = 15.5 MeV are compared to calculations performed by A. Deloff in figure 2.6.

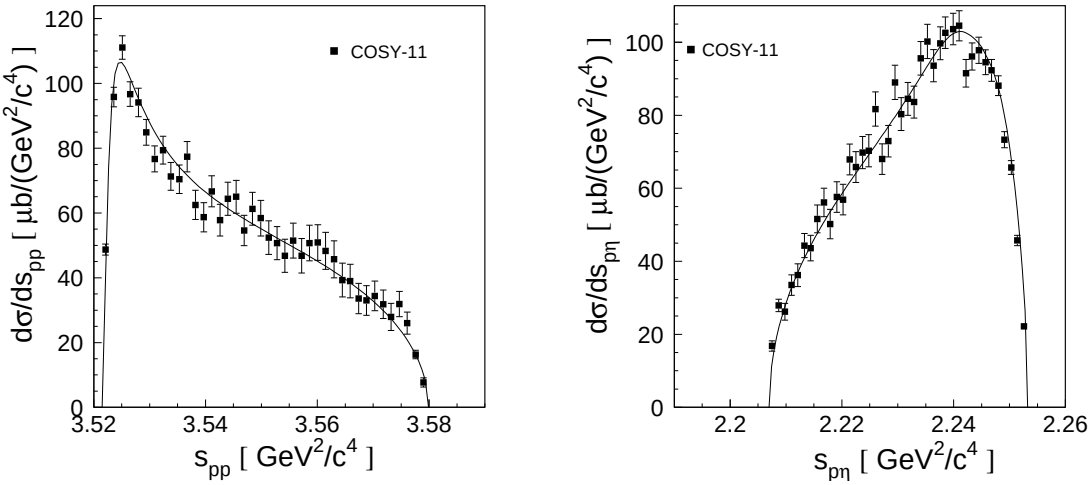

Figure 2.6: Distributions of the square of the proton-proton (s_{pp}) (left) and proton-η ($s_{p\eta}$) (right) invariant masses determined experimentally for the $pp \rightarrow pp\eta$ reaction (closed squares). The experimental data are compared to calculations performed assuming the linear energy dependence of the production amplitude as proposed by A. Deloff [13] depicted by solid lines.

The squared invariant mass distributions could be quite well reproduced by lifting the standard on-shell approximation in the enhancement factor and allowing for a linear energy

dependence in the leading ${}^3P_0 \rightarrow {}^1S_0 s$ partial wave amplitude [13]. Those calculations are in contradiction to the suggestion of Nakayama [12], giving evidence that higher partial waves play only a marginal role.

At this point, the observed enhancement could be explained by three different hypotheses:
i) a significant role of **proton-η interaction** in the final state,
ii) an **admixture of higher partial waves** or
iii) an **energy dependence of the production amplitude**.
Based on the $pp \rightarrow pp\eta$ data only, it is not possible to verify any of those models. These contingencies motivated the work presented in this thesis which is an analysis of a high statistics $pp \rightarrow pp\eta'$ reaction measurement in order to determine the distribution of events over the phase space for an excess energy of Q = 15.5 MeV the same one as selected before for the $pp \rightarrow pp\eta$ reaction. The comparison of the differential distributions for the proton-proton and proton-meson invariant masses in the η and η' production could help to judge between postulated explanations of the observed effect and may allow for a quantitative estimation of the proton-η and proton-η' interaction.
The experimental facility, the method of the analysis, and achieved results for the $pp \rightarrow pp\eta'$ reaction will be presented in the following chapters.

3. Experimental facility

The measurement of the $pp \to pp\eta'$ reaction was conducted using the cooler synchrotron COSY and the COSY-11 detector setup. Both facilities will be described in this chapter.

3.1 Cooler Synchrotron COSY

The COoler SYnchrotron (COSY) [17] is located at the Institute of Nuclear Physics of the Research Centre Jülich in Germany. The facility was designed to accelerate polarized and unpolarized proton and deuteron beams in the momentum range from 0.3 GeV/c up to 3.7 GeV/c. The sketch of the whole accelerator complex is presented in figure 3.1. The total length of the synchrotron ring is 184 meter. There are two straight 40 meter sections, and two bending sections with 24 dipole magnets.

The experimental installations at the synchrotron can be classified as two groups;
a) the detectors installed inside the COSY ring: WASA [40,41], COSY-11 [14–16], PISA [42], EDDA [43], COSY-13 [44], and ANKE [45] and
b) outside of the COSY ring at external beam lines: COSY-TOF [46], JESSICA [47], NESSI [48], GEM [49], MOMO [50], and HIRES [51].
Some of those experiments are already completed and no longer in operation (labelled in black) and the others are still in operation (labelled in green) in figure 3.1.

The COSY synchrotron is equipped with electron and stochastic cooling devices which are used to decrease the momentum and spatial spread of the beam [52].
In the case of electron cooling, the electrons with velocities equal to the nominal proton beam velocity are injected at a straight section of the synchrotron. This operation causes that faster protons are decelerated and slower ones are accelerated.
Stochastic cooling uses an electromagnetic device, the so called pick-up unit, which measures the beam deviation from the nominal position at one point of the accelerator and corrects it by transmitting a correction signal through the shortest way to the kicker unit at the other side of the beam pipe. It causes not only a shift to the nominal beam orbit, but also decreases the spread of the transversal and longitudinal momentum components [53, 54].

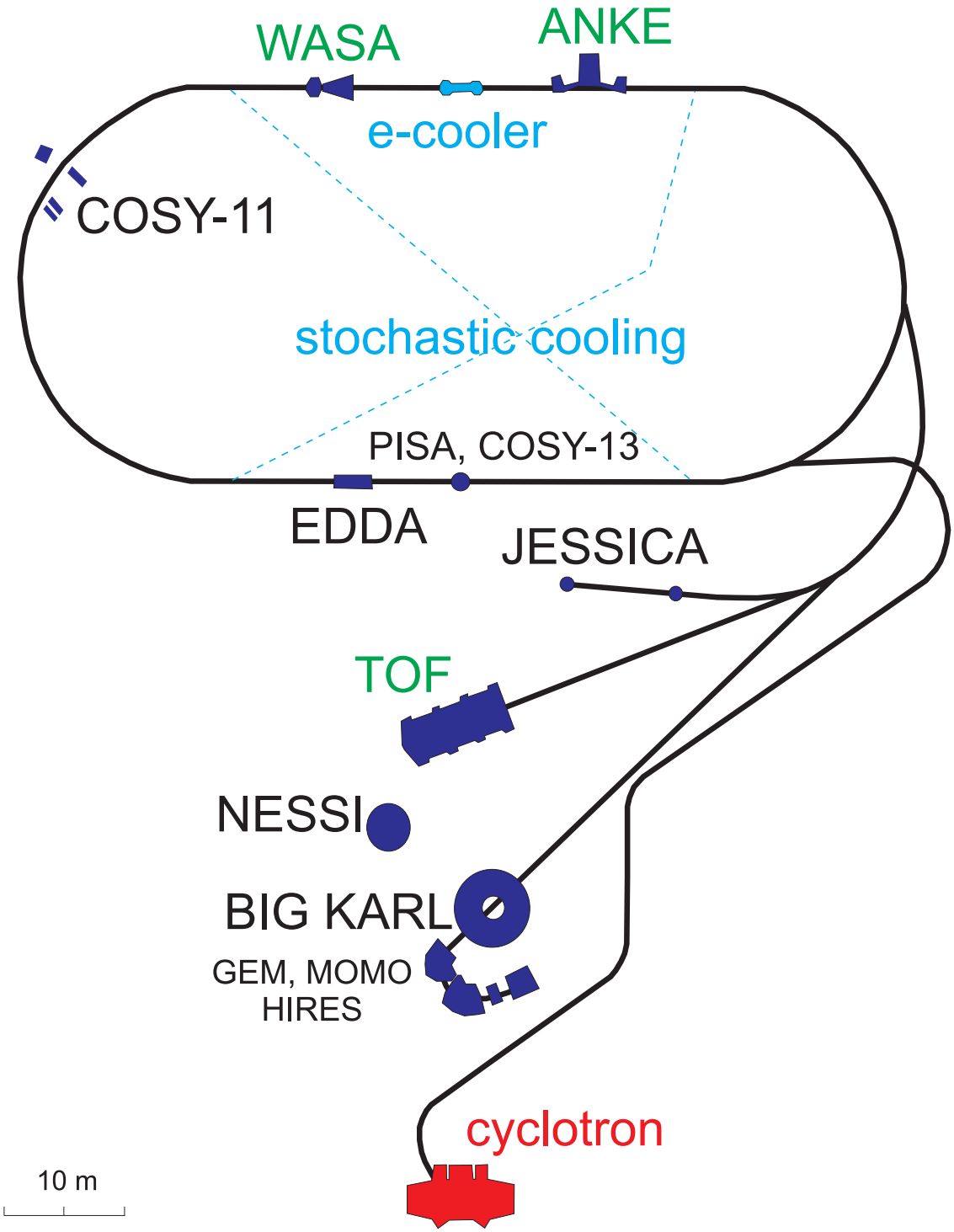

Figure 3.1: Schematic view of the floor plan of the COSY synchrotron. Marked in violet are internal-beam [14, 40, 42–45] and external-beam [46–51] detector setups. Facilities COSY-TOF, WASA and ANKE labelled in green are presently still in operation. The positions of electron and stochastic cooling devices are indicated and the stochastic cooling signal lines are presented by the light-blue dashed lines.

3.2 COSY-11 detector setup

The measurement of the $pp \to pp\eta'$ reaction is based on the registration of the two outgoing protons and reconstruction of their momenta. The η' meson is identified using the missing mass technique.

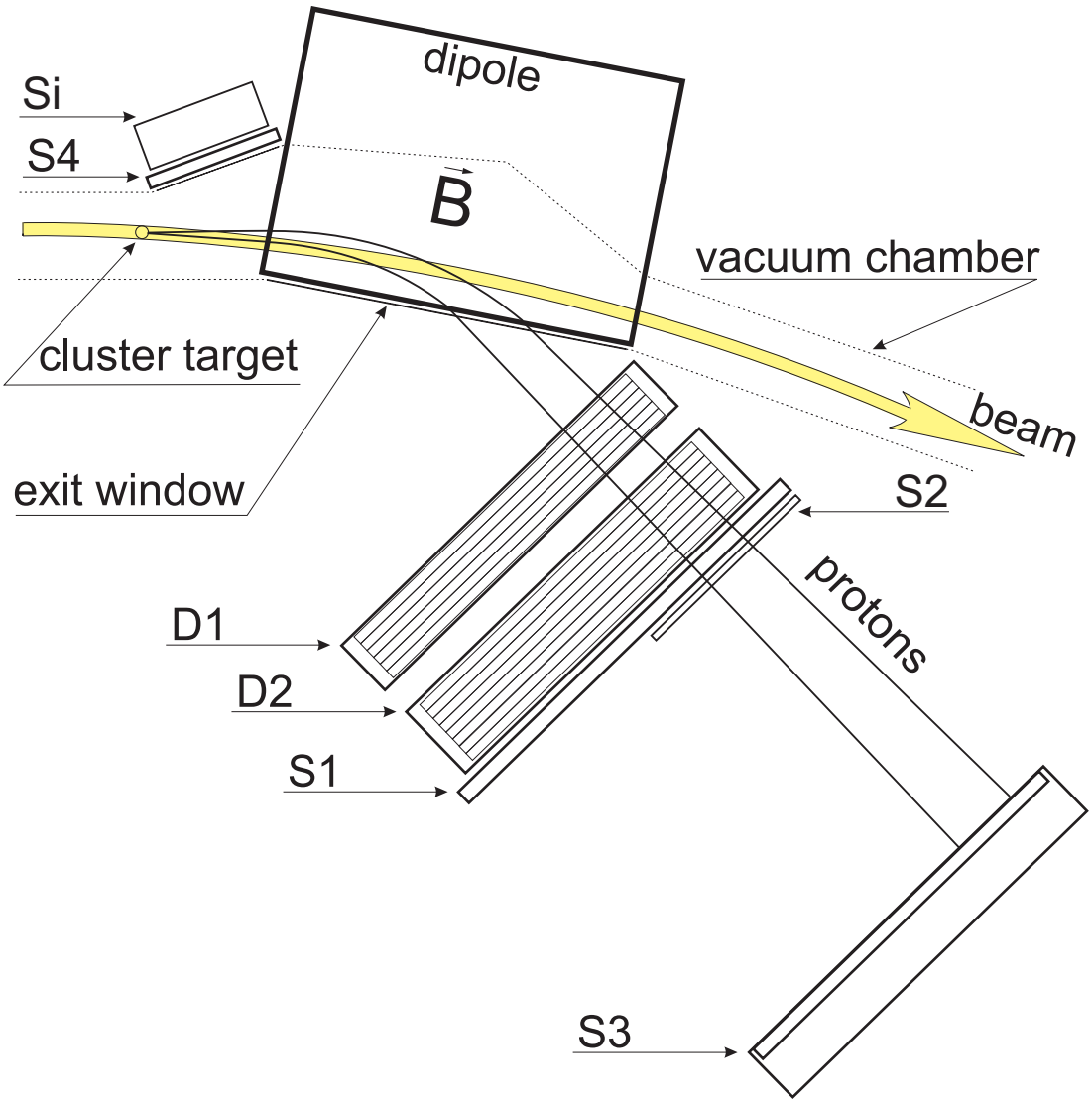

Figure 3.2: Schematic view of the COSY-11 detection facility [14]. Note, that only those detectors which were used during the measurement of the $pp \to ppX$ reaction are presented. Protons originating from the $pp \to ppX$ reaction are bent in the dipole magnetic field, and leave the vacuum chamber through the exit window. Afterwards they are detected in the two drift chambers D1 and D2, in the scintillator hodoscopes S1 and S2, and in the scintillator wall S3. The scintillation detector S4 and the silicon pad detector Si are used in coincidence with the D1, D2 and S1 detectors for the registration of the elastically scattered protons.

The COSY-11 facility is one of the internal detector setups installed inside the COSY synchrotron tunnel at a bending section of the ring. It is mounted next to one of the dipole magnets, and benefits from the dipole magnetic field which is used for the particle separation from the beam.

A schematic view of the COSY-11 apparatus is presented in figure 3.2. The figure illustrates also schematically the tracks of protons outgoing from the $pp \to ppX$ reaction. Two outgoing protons possessing smaller momenta than the beam momentum, are bent in the dipole magnetic field towards the detector system. They leave the vacuum chamber throughout the exit window made out of a 30 μm layer of aluminum and 300 μm of a carbon fiber carrier material with an averaged density of 2.1 g/cm^3 [14] and are detected using the drift chambers D1 and D2, the scintillator hodoscopes S1 and S2, and the scintillation wall S3[1].

The target[2] used during the experiment, was realized as a beam of H_2 molecules grouped inside clusters of up to about 10^6 atoms. The average density of the target was around $5 \cdot 10^{13}$ atoms/cm^2 [63]. It was installed in front of the dipole magnet as it can be seen schematically in figure 3.2.

The drift chambers D1 and D2 were used for the determination of the particles trajectories. Those two planar drift chamber stacks are spaced by 70 cm [14, 64]. Their active area is 1680 mm wide and 433 mm high. Drift chamber D1 (standing closer to the bending magnet) consists of six detection planes. The first two with vertical wires, two with wires inclined by $+31^o$ and two inclined by -31^o. The D2 drift chamber is built in the same scheme, but it is extended by two additional planes with vertical wires.

The wires in adjacent planes of each pair are shifted by half of the cell width to resolve the left-right position ambiguity with respect to the sense wire. The chosen configuration of the detection planes allows to perform the measurement of the horizontal and vertical coordinates and enables a unique multi-hit event identification [64].

A charged particle crossing the drift chambers produces gas ionization inside the drift cells, filled with a gas mixture of one to one argon and ethane at atmospheric pressure. The electron drift time to the sense wire is a measure of the distance between the passing particle track and the sense wire (see section 4.1). In the case of particle tracks oriented perpendicular to the detection planes, the maximum drift time corresponding to the maximum drift path of 20 mm equals to 400 ns.

[1] In the measurement of the meson production in the quasi-free $pd \to pnp_{spectator}X$ reaction dedicated neutron [55–58] and spectator [59–61] detectors were installed in addition. They were however not used for the measurement described in this thesis.

[2] The H_2 cluster target specifications are described in the references [62, 63]. The dimensions of the cluster target used during the measurement are described in details in chapter 7.

Determined particle trajectories in the data analysis are traced through the magnetic field of the dipole back to the target. Therefore, it is possible to reconstruct the momentum vectors of outgoing particles at the reaction point. The reconstruction of the momentum vectors of the registered particles combined with the information about the time-of-flight between the S1 and the S3 detectors allows for the calculation of the particle mass and by this the particle type identification.

The S1 scintillating hodoscope is built out of sixteen identical, vertically arranged modules, read out from both sides (top and bottom) by photomultipliers. The modules with $45 \times 10 \times 0.4$ cm^3 dimensions are arranged with small vertical overlap (1 mm [14,65]) in order to avoid "not covered" space in the geometrical acceptance. The S1 detector is used as the "start" for the time-of-flight measurement.

The S2 scintillating hodoscope, similar as S1, consists of sixteen scintillation modules with the dimension of $45 \times 1.3 \times 0.2$ cm^3 [14].

The S3 scintillating detector delivers the "stop" information for the time-of-flight measurement. It is built from one non-segmented scintillating wall with the dimension of $220 \times 100 \times 5$ cm^3. It is viewed by a matrix of 217 photomultipliers [14,66,67], occupying the edges of equilateral triangles with the sides of 11.5 cm.

The S4 scintillation counter together with the silicon pad detector (depicted in figure 3.2 as Si) are used for registration of the recoil protons from the proton-proton elastic scattering [14]. The silicon pad detector [14] consists of 144 pads with dimensions of $22.0 \times 4.5 \times 0.28$ mm^3. Each pad is read out separately.

3.3 Trigger logic

In the experiment two independent trigger branches were used, in order to detect the $pp \rightarrow pp\eta'$ and $pp \rightarrow pp$ reactions.
The main trigger used for the $pp \rightarrow pp\eta'$ reaction was based on the following conditions:

$$T_{pp\rightarrow pp\eta'} = (S1_{\mu\geq 2} \vee S1_{\mu=1,high} \vee S2_{\mu\geq 2} \vee S2_{\mu=1,high}) \wedge S3_{\mu\geq 2}, \tag{3.1}$$

where μ denotes the multiplicity of segments in the S1 and S2 scintillation hodoscopes, and the number of photomultipliers which have fired in the S3 detector. The subscript *high* stands for a high amplitude signal in the S1 and S2 detectors which was implemented for triggering events when two particles cross the same segment [67]. The hardware threshold for the high amplitude was set high enough to reduce the number of single particle events considerably, and low enough to accept most events (almost 100 %) with two protons passing through one segment of S1 [67].
The trigger used for the selection of elastic scattering reactions was based on the coincidence

between signals from the S1 and S4 detectors:

$$T_{pp\to pp} = S1_{\mu=1} \wedge S4, \tag{3.2}$$

where the S1 hodoscope was used for the registration of forward scattered protons and the S4 scintillation detector was registering recoil protons.
The detectors were positioned to cover a large part of the kinematics of the $pp \to pp$ elastic scattering. Due to the high rate of the $pp \to pp$ reaction only every 128'th event was registered for the further analysis. The number of the elastic scattering events was later used for the luminosity determination (see chapter 6).

4. Calibration of the detector setup

In this chapter the method used to calibrate the COSY-11 detectors and their relative settings will be presented. In particular, the time-space relation of the drift chambers and the procedure of time-of-flight calibration will be described. In addition, the procedure of monitoring the relative beam-target setting will be discussed.

4.1 Space-time relation for drift chambers

The drift chambers D1 and D2 consist of 6 and 8 planes of wires, respectively. They provide the information about the drift time of electrons (to the sense wires) produced along the trajectory of charged particles passing through the chambers. In order to reconstruct those trajectories one needs to establish a relation between drift time and distance between the particle track and the sense wire (Fig. 4.1 (left)).

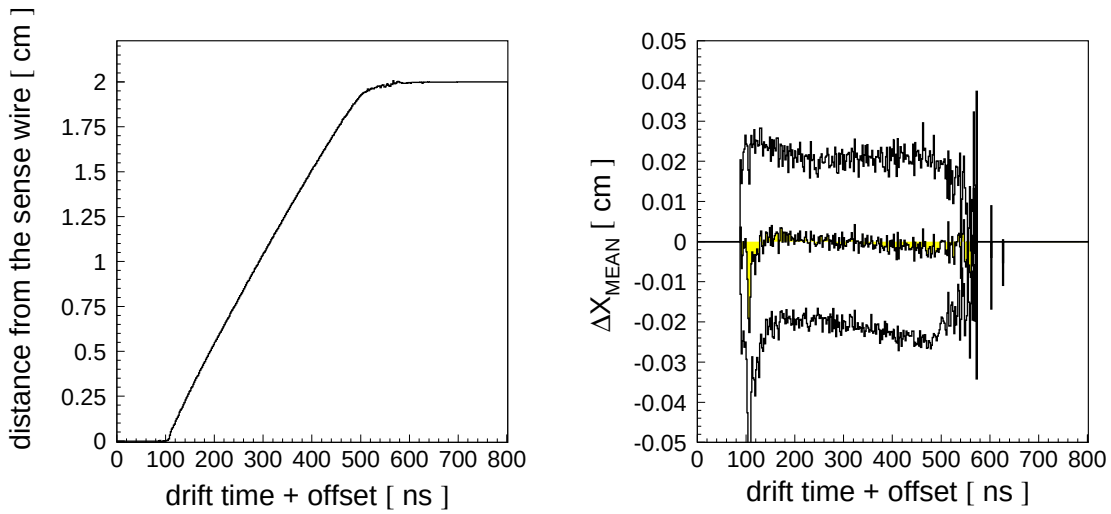

Figure 4.1: (Left panel) Time-space calibration - relation between the distance from the sense wire and the drift time. (Right panel) Corrections of the time-space relation, where the middle histogram represents the mean value of ΔX, the upper and lower histograms visualize one standard deviation (σ) of the ΔX distribution. See the text for the explanation of ΔX.

Due to the sensitivity of the drift velocity to the atmospheric pressure, humidity and gas mixture changes [68], the data used for the calibration procedure were divided into time intervals of about 3-8 hours, with a similar number of collected events. The calibration function was determined for each interval applying the procedure of iterative improvements [67]. Starting with an approximated function of the space-time relation, the distance X from the particle trajectory to the sense wire has been calculated. Then, a

straight line to the obtained points was fitted and further on, assuming that it corresponds to the real particle track, the deviation ΔX , between the measured distance of the particle track from the sense wire and the one from the fitting procedure was calculated. Next, having a certain amount of data, one could determine a mean value of ΔX as a function of the drift time (presented in figure 4.1 (right)). The ΔX_{MEAN} was subsequently used for a correction of the time-space relation. Next, the improved function has been used for the track reconstruction similarly as in the first step. The whole procedure was repeated until the corrections were smaller than the statistical uncertainty of the ΔX_{MEAN}.
The averaged spatial resolution of the drift chambers achieved in the experiment discussed in this thesis amounted to 250 μm (rms).

4.2 Time-of-flight calibration of scintillator detectors

The scintillator detectors S1 and S3 "start" and "stop", respectively, are used for the time-of-flight measurement. S1 consists of 16 scintillator plates with photomultiplier readout from both sides, and S3 is a scintillator wall read out by a 217 photomultipliers matrix. In order to obtain the proper information about the time-of-flight between both detectors, one needs to determine time "offsets" for all photomultipliers i.e. the relative differences in transition time of the signal from the photomultiplier to the TDC unit.
Let us denote t_{S1} as the real time when a particle crosses the S1 detector and t_{S3} when it crosses S3. Then, the time-of-flight can be calculated as follows: $tof_{S1-S3} = t_{S3} - t_{S1}$.
The measured TDC values for a single photomultiplier in S1 and S3 detectors read:

$$TDC_{S1} = t_{S1} + t_y + t^{S1}_{walk}(PM) + t^{S1}_{offset}(PM) - t_{trigger}, \tag{4.1}$$

$$TDC_{S3} = t_{S3} + t_{pos} + t^{S3}_{walk}(PM) + t^{S3}_{offset}(PM) - t_{trigger}. \tag{4.2}$$

In both equations the time stamp $t_{trigger}$ (denoting the time of the trigger signal) is identical. The index y corresponds to the distance between hit position and the edge of the scintillator close to the given photomultiplier in the S1 detector and *pos* stands for the distance between the hit position and the photomultiplier in the S3 detector. The abbreviation t_{walk} denotes the corrections for the $time - walk$ effect, i.e. the signal time dependence on the signal amplitude [69]. Any dependence of t_y is cancelled by taking the average between the times measured by the upper and lower photomultipliers [67] and this can be calculated from the known trajectories. Thus, the only unknown variables are the time offsets t_{offset} for both detectors. For a first approximation, the time difference in the S1 detector can be achieved by taking into account signals from the particles crossing the overlapping parts of the modules. Next, for the S3 detector the time offset can be extracted from the comparison between $tof_{S1-S3} = t_{S3} - t_{S1}$ and the time-of-flight calculated from the particle momentum reconstructed via curvature in the magnetic field

(tof_{rec}). Then, iteratively, using the obtained S3 offset one can determine the time offsets for the S1 detector. After two iterations, the time offsets for both detectors can be established. As an example, the distribution $\Delta t(PM_{ID}^{S3})$ determined as

$$\Delta t(PM_{ID}^{S3}) = tof_{S1-S3}(PM_{ID}^{S3}) - tof_{rec}$$

for a group of photomultipliers of the S3 detector are presented in figure 4.2.

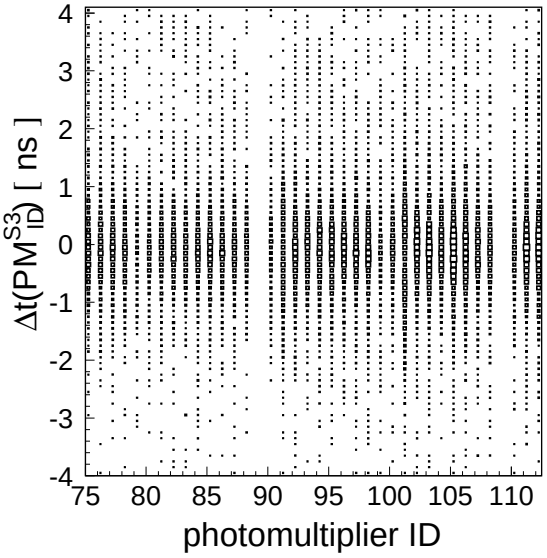

Figure 4.2: Distribution of the time difference between the time tof_{rec} calculated from the reconstructed particle momentum and the measured time tof_{S1-S3} between the S1 detector and a particular photomultiplier in the S3 detector, as a function of the photomultiplier ID in the S3 detector. As achieved after second iteration, the figure depicts only a fraction of PM's of the S3 detector (75-112).

The time offsets for the photomultipliers in the S3 detector are obtained on the basis of the time differences between tof_{S1-S3} and tof_{rec} presented in figure 4.2. They were adjusted such that this difference is equal to zero.

4.3 Monitoring of relative beam-target settings

Possible changes of the position where the beam crosses the target could have significantly influenced the momentum reconstruction and as a consequence could worsen the determination of the mass of the undetected particle. Therefore, it is important to monitor the position of the beam and target overlap. The center of the beam-target overlap can be determined from the momentum distribution of the elastically scattered protons [70].

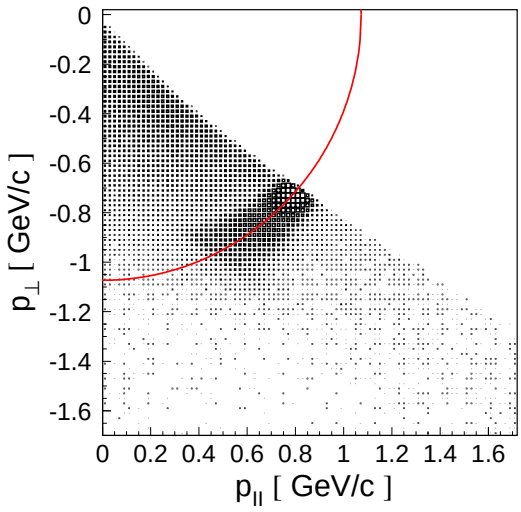

Figure 4.3: The distribution of the perpendicular $p_\perp$ versus parallel $p_\parallel$ momentum components for $pp \rightarrow pp$ elastic scattering events at a beam momentum of 3.260 GeV/c. The solid line corresponds to the kinematical ellipse. Changes of the event density along the kinematical ellipse reflect the angular dependence of the cross section for the $pp \rightarrow pp$ reaction.

The mean value of the distance between the expected kinematical ellipse and the experimental points (shown in figure 4.3) may be used as a measure for the deviation of the center of the interaction region from its nominal position ($\Delta center$). A pictorial definition of $\Delta center$ is presented in figure 4.4 and the beam-target geometrical conditions are depicted in figure 4.5. By assuming a wrong interaction center the reconstruction results in a wrong momentum determination and the $pp \rightarrow pp$ events are not centered around the expected kinematical ellipse.

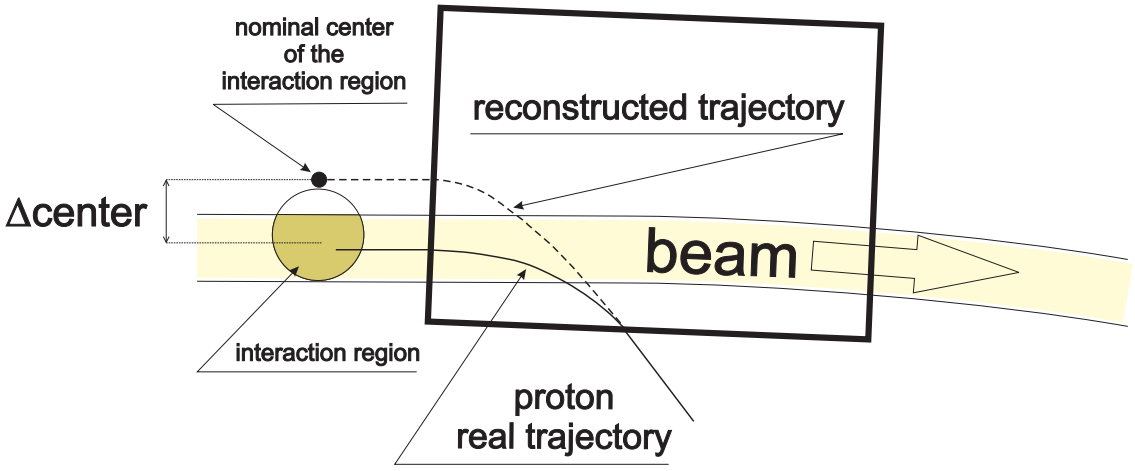

Figure 4.4: Pictorial definition of the deviation of the center of the interaction region from its nominal position ($\Delta center$).

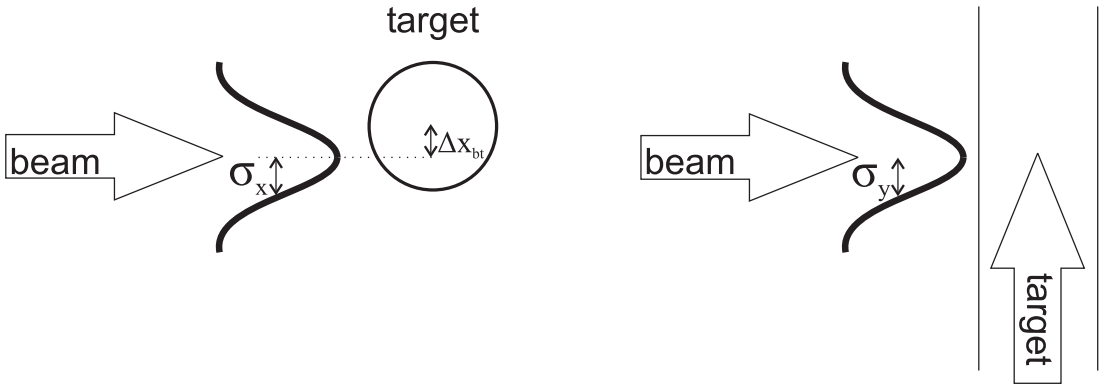

Figure 4.5: Schematic view of the relative target and beam settings. Left panel depicts the view from above, right presents a side view. σ_X and σ_Y denote the horizontal and vertical standard deviations of the assumed Gaussian distributions of the proton beam density, respectively. $\Delta_{X_{bt}}$ denotes the distance between the centers of the proton target and beam. The figure is adapted from [70].

In the left panel of figure 4.6 the mean distance of experimental $pp \to pp$ events from the expected kinematical ellipse is shown as a function of $\Delta center$ assumed in the analysis. As can be seen, the center of the interaction region differs by 0.45 cm from the nominal one.

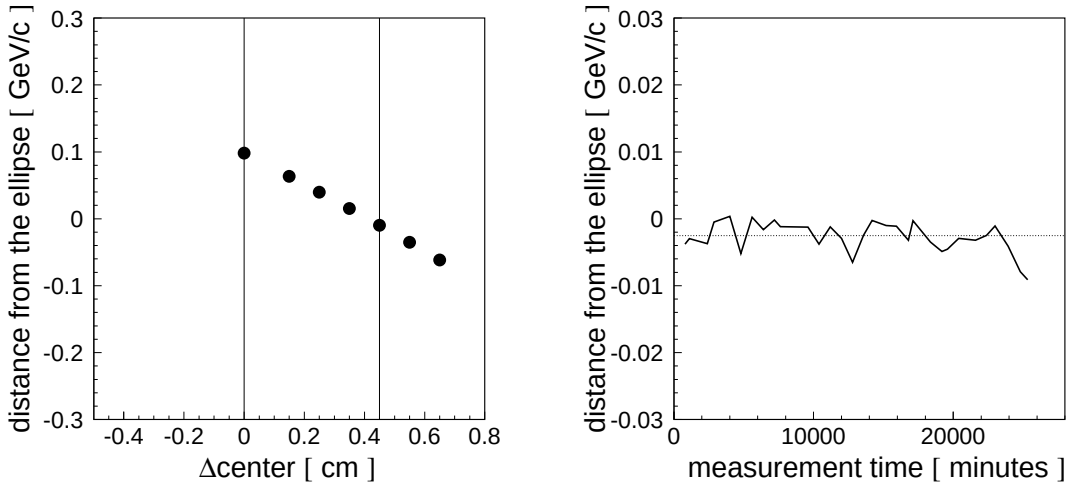

Figure 4.6: (Left panel) The distance between the expected ellipse and the center of experimental distribution on the ($p_\perp$,$p_\parallel$) plot (figure 4.3) versus the deviation of the center of the interaction region from its nominal position ($\Delta center$). (Right panel) The deviation of the distance from the kinematical ellipse as a function of the time of the measurement. The mean value of the distance from the ellipse has been plotted for 13 hours intervals. In the analysis the value of $\Delta center$ was set to 0.45 cm.

In the right panel of figure 4.6 it is demonstrated that the beam-target conditions were stable during the course of the experiment. Fluctuations seen in the figure are within the

statistical error in the determination of the mean value of the distance from the ellipse. The variations are at a level of 10^{-3} and, as can be inferred from the plot presented in the left panel of figure 4.6, correspond to shifts of the interaction center by less than 0.01 mm. Thus, the variations of the center of the interaction region can be safely neglected in the further analysis.

5. Identification of the $pp \to pp\eta'$ reaction

In the following chapter the method of identifying the $pp \to pp\eta'$ reaction will be described.

5.1 Identification of protons

The measurement was based on the registration of two outgoing protons originating from the $pp \to ppX$ reaction.

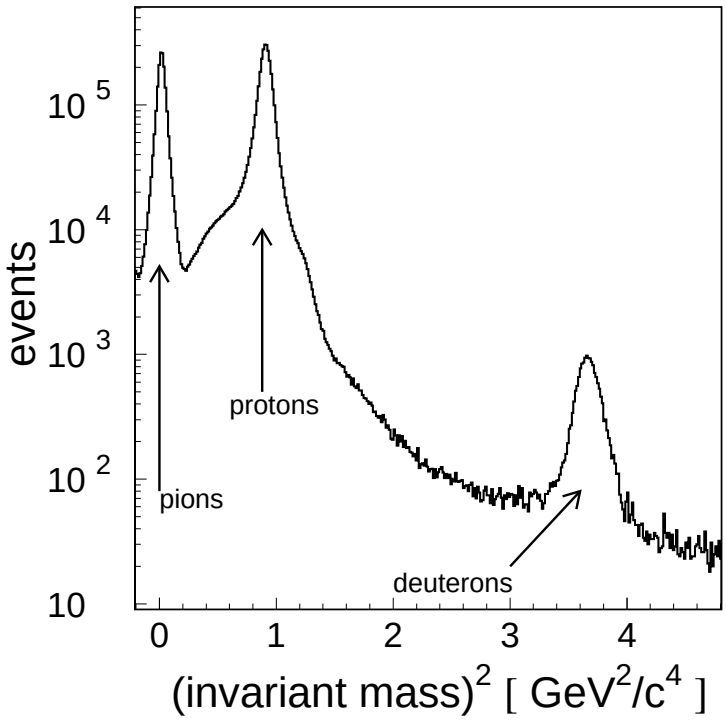

Figure 5.1: Distribution of the squared invariant mass of the registered particles. (Note the logarithmic scale on vertical axis.) Signals from measured pions, protons, and deuterons are easily distinguished.

After choosing only two-track events, the protons were identified by the determination of their rest masses. The particle mass was calculated according to the following formula:

$$m^2 = \frac{\vec{p}^{\,2}(1-\beta^2)}{\beta^2}, \tag{5.1}$$

where $\vec{p}$ and β are denoting the momenta and velocities of particles, respectively, which were determined in an independent way ($\vec{p}$ from the curvature of the trajectory in the

dipole and β from the time of flight between S1 and S3). The distribution of the squared masses of the particles is shown in figure 5.1. Clearly visible are signals from pions, protons and deuterons.
For the further analysis, particles with reconstructed masses in the range from 0.2 to 1.5 GeV^2/c^4 were assumed to be protons.

5.2 Identification of the η' meson

In the present experiment the decay products of the η' meson were not measured, therefore it was impossible to identify its production on an event-by-event basis. Even in experiments detecting all decay products an unambiguous identification of a single "η' production event" is not possible, but the background would be much smaller.

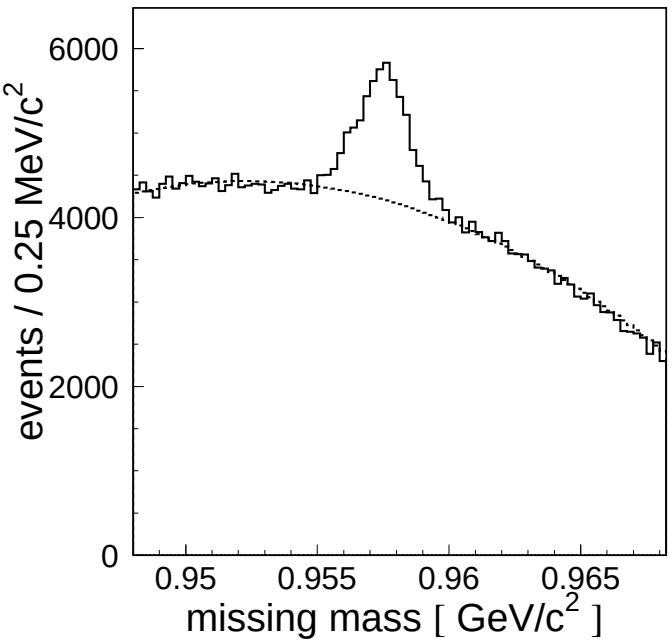

Figure 5.2: Missing mass spectrum for the $pp \to ppX$ reaction measured at a beam momentum of $P_B = 3.260$ GeV/c. The peak originating from the $pp \to pp\eta'$ reaction is clearly seen on top of a multi-pion production background. The dashed line corresponds to a fit with a second order polynomial to the data outside the signal from the η' meson.

The number of $pp \to pp\eta'$ events was determined using the missing mass technique. This method is based on the knowledge of the protons four-momenta before and after the reaction. Denoting: $\mathbb{P}_b = (E_b, \vec{p}_b)$, $\mathbb{P}_t = (E_t, 0)$, $\mathbb{P}_1 = (E_1, \vec{p}_1)$ and $\mathbb{P}_2 = (E_2, \vec{p}_2)$ as the

four-momenta of the proton beam, proton target, and first and second outgoing proton, respectively, one can use the following formula, in the case of the $pp \to ppX$ reaction, to calculate the mass m_X of the unregistered particle:

$$m_X^2 = E_X^2 - \vec{p}\,_X^2 = (\mathbb{P}_b + \mathbb{P}_t - \mathbb{P}_1 - \mathbb{P}_2)^2 =$$
$$= (E_b + E_t - E_1 - E_2)^2 - (\vec{p}_b + \vec{p}_t - \vec{p}_1 - \vec{p}_2)^2. \quad (5.2)$$

In figure 5.2 the missing mass spectrum determined experimentally for the $pp \to ppX$ reaction for the whole data sample is presented. The spectrum includes a broad distribution from multi-meson production and the well defined peak originating from the η' meson production.

The smooth behaviour of the experimental multi-pion production background, which could be verified by Monte Carlo simulations studies (see section 9.2), allows for a simple polynomial fit. The knowledge of the smooth behaviour of the cross section [60, 71], assures that in the range of the signal, the multi-pion background should be flat.

The dashed line in figure 5.2 corresponds to a second order polynomial fitted to the experimental background. Indeed, it can be seen that the fit reproduces the shape of the background satisfactory well.

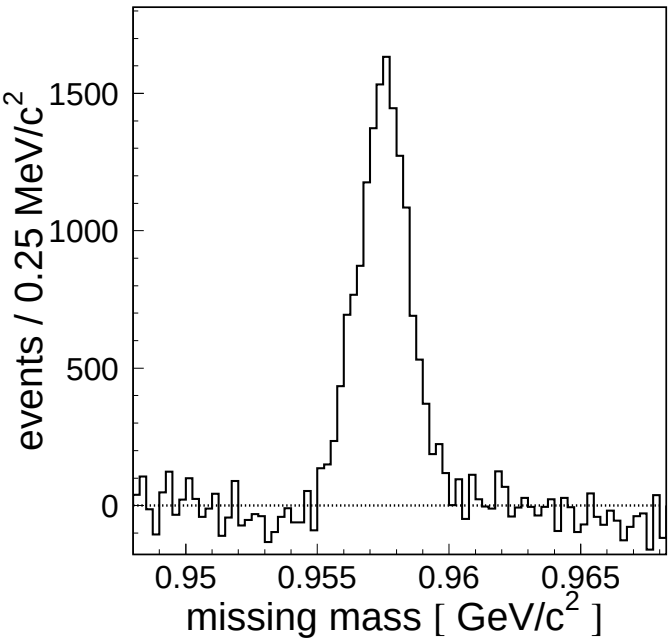

Figure 5.3: Result of the background subtraction using the second order polynomial fit presented in figure 5.2 as a dashed line.

In figure 5.3 the experimental missing mass spectrum after the background subtraction is presented. The background was approximated by a second order polynomial fit as depicted in figure 5.2 by a dashed line. The total number of registered and reconstructed $pp \to pp\eta'$ reactions amounts to about 15000.
Here, the statistics achieved in the measurement is only illustrated and the possibility of the background determination is shown. A detailed discussion of the subtraction of the multi-pion production background for differential cross sections will be comprehensively described in section 9.2.

6. Luminosity determination

In order to determine the absolute values of the differential cross sections, the luminosity (L) integrated over the measurement time has to be established. For that purpose, the analysis of the $pp \rightarrow pp$ reaction, in order to establish the number of elastic scattering events was performed.
A schematic view of the COSY-11 detector setup with superimposed tracks of elastically scattered protons is shown in figure 6.1.

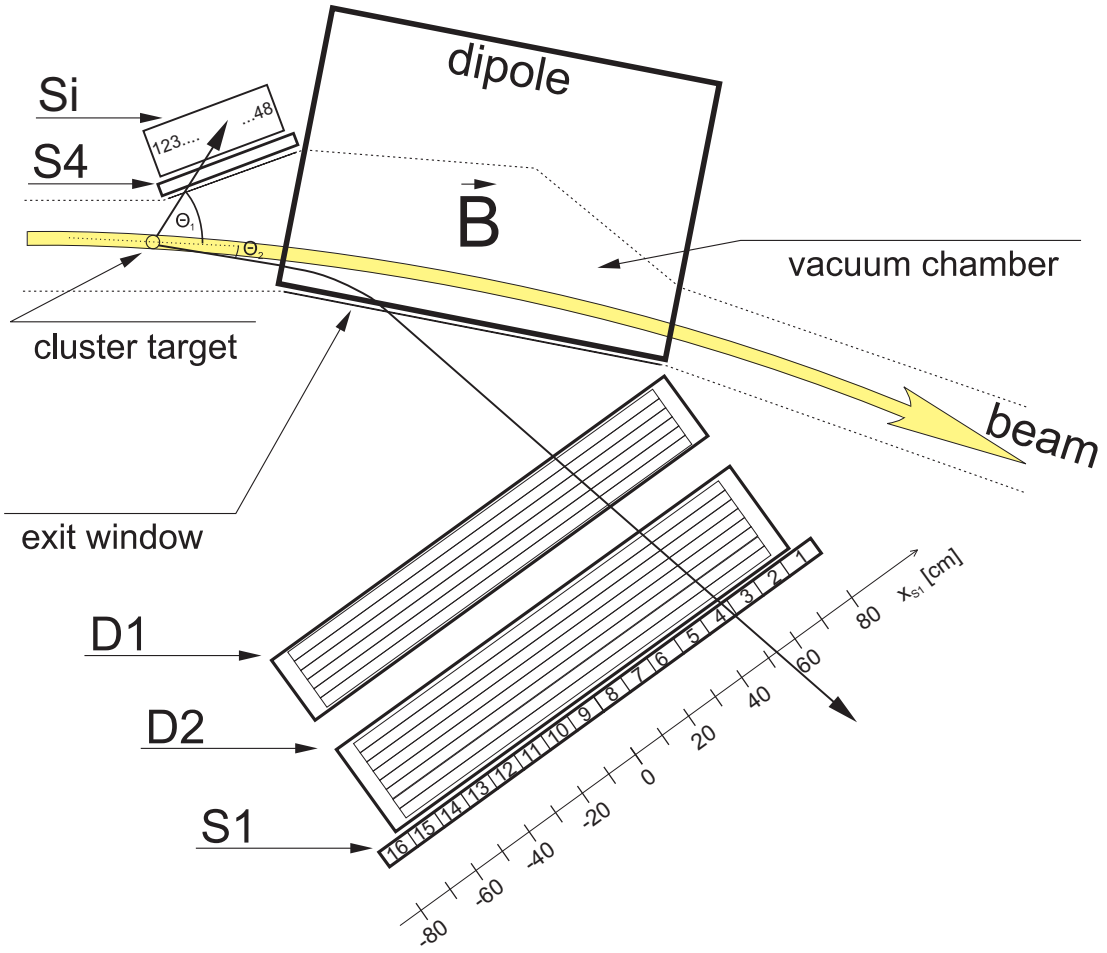

Figure 6.1: Schematic view of the COSY-11 apparatus presenting the detectors used for the registration of the $pp \rightarrow pp$ elastic scattering. The superimposed lines show an example of trajectories from elastically scattered protons with the laboratory angles θ_1 and θ_2. One can compare this figure to figure 3.2. The x_{S1} axis indicates the size of detector modules (for further description see text).

One can evaluate the luminosity (L) according to the formula:

$$\frac{\Delta N(\theta_2^*)}{\Delta\Omega^*(\theta_2^*)} \;=\; \frac{d\sigma^*}{d\Omega^*}(\theta_2^*) \;\cdot\; L, \tag{6.1}$$

where $\frac{d\sigma^*}{d\Omega^*}(\theta_2^*)$ denotes the known differential cross section [72] and $\Delta N(\theta_2^*)$ indicates the number of elastically scattered protons at a solid angle $\Delta\Omega^*$ around the proton emission angle θ_2^* in the centre-of-mass system. In the further analysis, the available range of the θ_2^* angle (44^o to 66^o) was divided into 11 bins with a width of 2^o. The tracks of elastically scattered protons resulting in signals in the S1 detector with a coincident signal in S4 from the second proton covers the horizontal axis of the S1 detector, marked in figure 6.1 as x_{S1}, from 40 cm to 75 cm, which corresponds to a θ_2^* angle range from 44^o to 66^o.

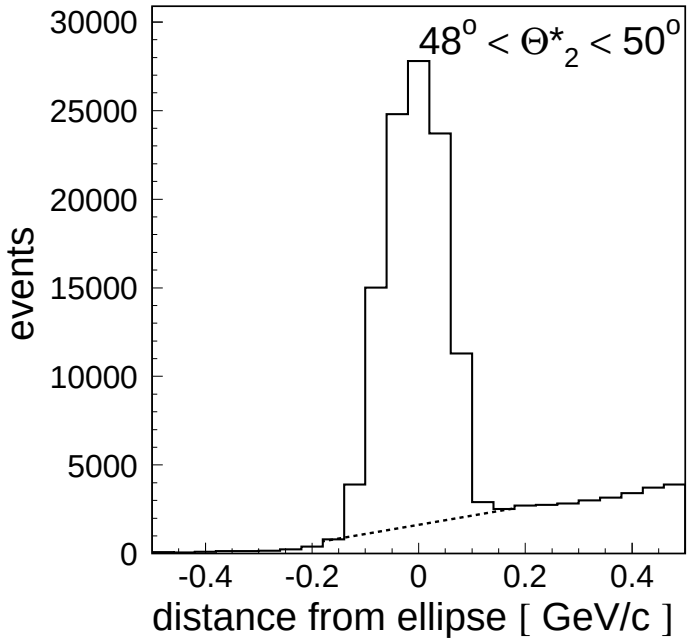

Figure 6.2: Projection of the event distribution along the kinematical ellipse for a centre-of-mass proton scattering angle of θ_2^* in the range from 48^o to 50^o, corresponding to the range in the S1 detector from $x_{S1} = 67.0\ cm$ to $x_{S1} = 70.0\ cm$.

As an example, the distribution of elastically scattered protons at the θ_2^* angular range from 48^o to 50^o is presented in figure 6.2. This distribution shows the projection of the experimental data along the kinematical ellipse. The number of events (reduced by the background indicated by the dashed line) is used for the calculation of the luminosity.
The signal from elastically scattered protons can be clearly separated from the flat multi-pion scattering background. The solid angle $\Delta\Omega^*$ or the certain angular bin, is calculated

using the Monte-Carlo method, as follows:

$$\Delta\Omega^* \;=\; \frac{4\pi\ N_{accepted}}{2\ N_0}\ [sr], \tag{6.2}$$

where N_0 stands for the number of proton-proton elastic scattering events in the corresponding angular range and $N_{accepted}$ constitutes the number of events in the considered bin of the θ_2^* angle, which could be registered and identified. In particular, the analysis in the following manner was done. First, $N_0 = 2 \cdot 10^7$ events has been generated, calculating the response of the COSY-11 detectors, and then those events have been analysed using procedures applied for the experimental data evaluation in order to determine the number of $N_{accepted}$ events for each θ_2^* angle interval.

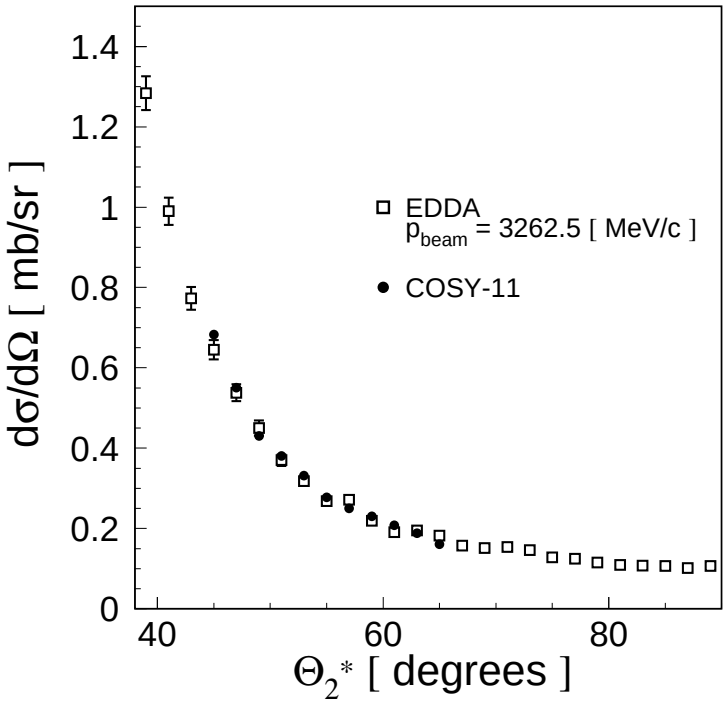

Figure 6.3: Differential cross section for the proton-proton elastic scattering. The result of this thesis (closed circles) measured at a beam momentum of $P_B = 3.260$ GeV/c was scaled in amplitude to the cross section measured by the EDDA collaboration shown by open squares [72].

Figure 6.3 indicates the angular distribution of the differential cross section for elastic proton-proton scattering obtained in the experiment (closed circles). The amplitude of that distribution was fitted to the data of the EDDA experiment including only one free parameter being the integrated luminosity (see eq. 6.1). The extracted integrated luminosity for the experiment described in this thesis amounts to $\mathbf{L \;=\; (5.859 \pm 0.055)\ pb^{-1}}$.

The knowledge of the luminosity value will allow for the overall normalization of the derived differential cross section as a function of the s_{pp} and $s_{p\eta'}$ invariant masses, angular distributions and total cross section which will be discussed in chapter 10.

7. Determination of the spread and the absolute value of the beam momentum

In order to perform realistic simulations of the studied reactions, in particular to determine the acceptance and to calculate the covariance matrix, it is mandatory to know the absolute value and the spread of the beam momentum. The discussed measurement of the $pp \to pp\eta'$ reaction was nominally performed at the same value of excess energy Q as the $pp \to pp$ reaction measurement with Q = 15.5 MeV which corresponds to a nominal proton beam momentum of $P_B = 3.257$ GeV/c.
The precision of the absolute beam momentum adjustment of the COSY synchrotron is about 10^{-3} [52] which in this case corresponds to ∼3 MeV/c.
The beam momentum dependence of the mean value of the missing mass distribution presented in figure 5.3, was studied in order to determine the actual value of the beam momentum more accurate.
The beam momentum was calculated using the formula:

$$m_X = \sqrt{s} - 2m_p = \left(2m_p^2 + 2m_p\sqrt{P_B^2 + m_p^2}\right)^{1/2} - 2m_p, \tag{7.1}$$

where $\sqrt{s}$ denotes the total energy in the centre-of-mass frame, P_B stands for the proton beam momentum, and m_p corresponds to the proton mass.
The beam momentum of $P_B = 3.260$ GeV/c has been determined by adjusting the P_B such that the mean value of the missing mass peak is equal to the η' meson mass. The determined value of the beam momentum differs by 0.003 GeV/c from the nominal one. This deviation is in agreement with results of analogous analysis performed in previous measurements [67].
The determined value of the excess energy amounts to **(Q = 16.39 ± 0.01 ± 0.4) MeV**, where the errors indicate statistical and systematic uncertainty, respectively. The dominating systematic uncertainty was established in [9] and the statistic uncertainty of the excess energy was determined using the following formula:

$$\Delta Q = \sqrt{\left(\frac{dQ}{dP_B}\right)^2 \cdot (\Delta P_B)^2}, \tag{7.2}$$

where ΔP_B was obtained from the linear relation to the missing mass as described in [67].

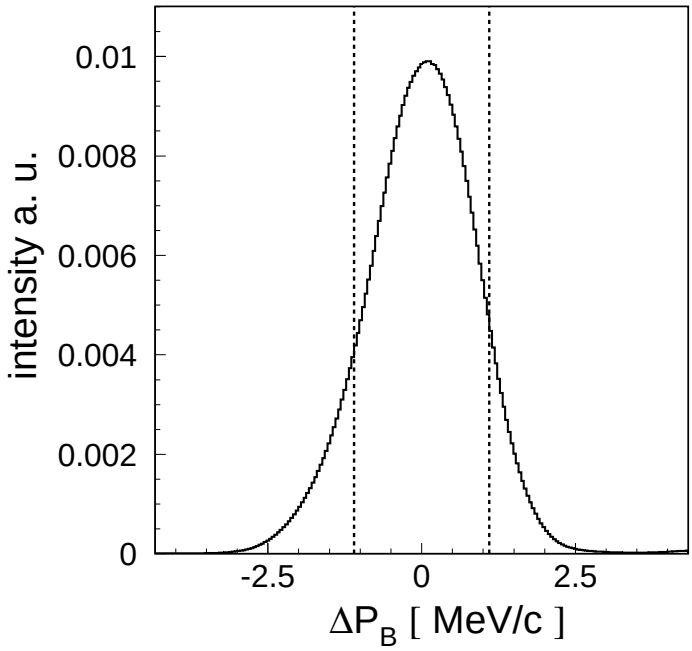

Figure 7.1: Spectrum of the beam momentum distribution integrated over the whole measurement time. The value of $\Delta P_B = 0$ corresponds to a beam momentum of 3.260 GeV/c. The dashed lines mark the beam momentum dispersion for the extended 9 millimeter target used in this experiment.

After the determination of the real value of the absolute beam momentum, now its spread will be determined. One can calculate the beam momentum spectrum from the frequency spectrum of the COSY beam (Schotky spectrum measured during the experiment) using the below formula [73]:

$$\frac{\Delta f}{f} \;=\; \eta_B \cdot \frac{\Delta P_B}{P_B}, \tag{7.3}$$

where f and P_B denote beam frequency and beam momentum, respectively, η_B is a parameter which depends on the beam optics, i.e. the electric and magnetic fields in the synchrotron. During the experiment, the η_B parameter was established to be $\eta_B = 0.12$ [74]. The spectrum of the beam momentum obtained during the experiment is shown in figure 7.1.

The dispersion of the beam momentum depends on the magnetic field along the ring. Protons on the outer routes have a "longer way" than those on the inner side of the beam, and the trajectories are different from the nominal value. When at a certain point the particle position deviates by Δx from the nominal (x_0) position and possesses the relative momentum deviation $\Delta P_B/P_B$, one can relate this value by means of the known dispersion

(D) using the following formula:

$$\Delta x = D \cdot \frac{\Delta P_B}{P_B}, \tag{7.4}$$

where $D = \beta \cdot D_{mod}$ with $D_{mod} = 14\ m$ [74,75] and the particle velocity β. Applying in the upper formulas the value of the beam momentum $P_B = 3.260$ GeV/c, $\beta = 0.961$, and using a 9 millimeter wide target, one obtains $\Delta P_B = 1.1$ MeV/c. This value is depicted in figure 7.1 as the area between the dashed lines. Thus, the maximum beam momentum spread in the interaction point is $\Delta P_B = \pm 1.1$ MeV/c.

8. Fine tunning of the relative dipole-chamber settings

In section 4.1 a space-time calibration of the drift chambers was described. In this chapter a procedure for the determination of their position relative to the COSY-11 dipole will be shown. For this purpose, the missing mass method for the $pp \rightarrow ppX$ and the kinematical ellipse for the $pp \rightarrow pp$ reaction, as described in the previous chapters, will be used.

The proper knowledge about the position of the drift chambers is needed in order to achieve the optimal resolution for the momentum reconstruction. In the horizontal plane the position of the drift chambers stack can be defined by two variables: the horizontal shift of the chambers Δx and their inclination $\Delta\alpha$.

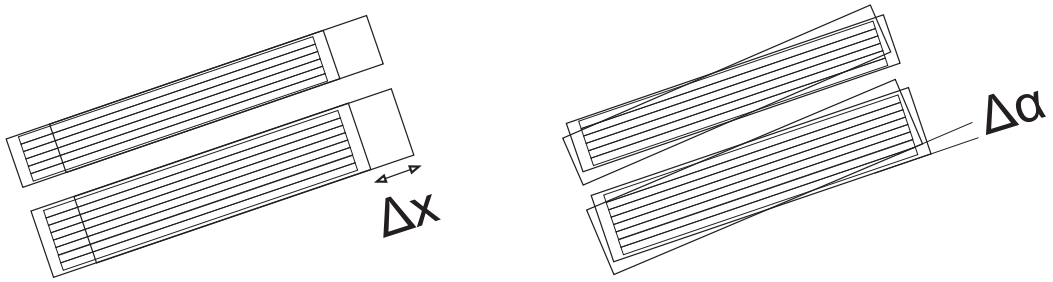

Figure 8.1: Schematic view (from top) with the pictorial definitions of the horizontal shift of the chambers Δx and their inclination $\Delta\alpha$. These parameters were used in the analysis to determine the proper arrangement of the D1 and D2 drift chambers relative to the COSY-11 dipole.

The parameters Δx and $\Delta\alpha$ influence the reconstruction of particle momenta and further more indirectly influence the missing mass resolution. In order to fix these parameters, an analysis of the proton elastic scattering events was performed, since the distribution of the perpendicular $p_\perp$ versus parallel $p_\parallel$ momentum components for the $pp \rightarrow pp$ reaction is sensitive to changes of the position of the drift chambers. The distribution of the $p_\perp$ versus $p_\parallel$ momentum components for the $pp \rightarrow pp$ elastic scattering determined at a beam momentum of 3.260 GeV/c, presented earlier in chapter 4.3, is shown in figure 8.2. In the left panel, the situation when the parameters are properly adjusted is presented. In the right panel the situation is shown when the inclination $\Delta\alpha$ was changed by $\sim 0.9^o$. Studies with a variation of $\Delta\alpha$ in the range from -0.9^o to 0.9^o and of Δx ranging from 0.0 cm to 1.0 cm were performed, where simultaneously the $p_\perp$ versus $p_\parallel$ spectrum and the changes of the width of the η' peak in the missing mass spectra were controlled.

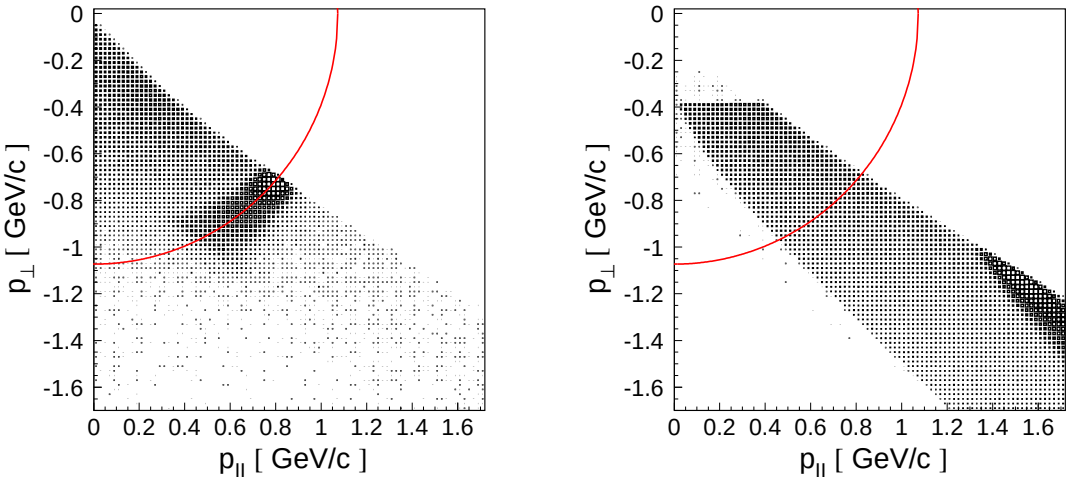

Figure 8.2: Distributions of the perpendicular $p_\perp$ versus the parallel $p_\parallel$ momentum components of measured protons for $pp \to pp$ elastic scattering events at a beam momentum of 3.260 GeV/c. The solid line corresponds to the kinematical ellipse where the elastically scattered events are expected. The distribution is shown for $\Delta\alpha = 0.04^o$ (left), and for $\Delta\alpha = -0.9^o$ (right), respectively.

The lowest width of the missing mass peak (see Fig. 5.2) and the best fit of the event distribution to the kinematical ellipse for the $pp \to pp$ elastic scattering distribution (see left panel of figure 8.2) has been found for the values of $\Delta x = 0.45$ cm and $\Delta\alpha = 0.04^o$. A comparison of the left and right histograms in figure 8.2 shows the sensitivity of this distribution to the parameter $\Delta\alpha$, which could be determined within an accuracy of better than 0.01^o.

9. Evaluation of the differential distributions

9.1 Kinematical fit

In order to search for small effects like proton-meson interaction on the population density of the phase-space, it is of importance to account for any possible changes of the measured distributions due to the finite resolution of the detector system, which may alter the shape of the spectrum especially close to the kinematical limit. Therefore, one must include the experimental resolution in the theoretical calculations and in order to improve the effect of the resolution a kinematical fitting of the data was performed. Both procedures require the knowledge of the covariance matrix.

In order to calculate the covariances and variances between each combination of the registered proton momentum components, $2 \cdot 10^7$ reactions of the type $pp \to pp\eta'$ have been generated including all arrangements and conditions from the experiment. Then, the whole simulated sample of events has been analysed with the same procedures as used for the experimental data. In this step for each simulated event the pair of the real (generated) protons momenta $\vec{P}_{1,gen}$, $\vec{P}_{2,gen}$ and the pair of momenta reconstructed from the simulated response of the detectors: $\vec{P}_{1,rec}$, $\vec{P}_{2,rec}$ are accessible. The available kinematical information about an event may be expressed in form of the six dimensional momentum vector: $P = [p_{1x}, p_{1y}, p_{1z}, p_{2x}, p_{2y}, p_{2z}]$ including the components of the reconstructed momenta of both protons $P_{1,rec} = [p_{1x}, p_{1y}, p_{1z}]$ and $P_{2,rec} = [p_{2x}, p_{2y}, p_{2z}]$. The covariance between the i^{th} and j^{th} components of P was determined as the average of the product of deviations between the reconstructed and generated values. The formula used to establish the covariance matrix elements, reads as follows:

$$cov(i,j) = \frac{1}{N}\sum_{n=1}^{N}(P^n_{i,gen} - P^n_{i,recon})(P^n_{j,gen} - P^n_{j,recon}), \tag{9.1}$$

where $P^n_{i,gen}$ and $P^n_{i,recon}$ stand for the generated and reconstructed values of the i^{th} component of the vector P from the n^{th} event.
Due to the inherent symmetries of the covariance matrix ($cov(i,j) = cov(j,i)$) and since the measured protons are indistinguishable, there are only 12 independent values which determine the 6×6 error matrix unambiguously [9].
The covariance matrix (in units of $\mathrm{MeV}^2/\mathrm{c}^4$) determined for the $pp \to pp\eta'$ reaction looks as follows:

$$
\begin{array}{c}
\begin{array}{cccccc} p_{1x} & p_{1y} & p_{1z} & p_{2x} & p_{2y} & p_{2z} \end{array} \\
\left[\begin{array}{cccccc}
10.3 & -0.1 & -19.6 & 7.6 & -0.0 & -13.0 \\
- & 6.2 & 0.1 & - & 0.1 & 0.0 \\
- & - & 43.0 & - & - & 21.7 \\
- & - & - & - & - & - \\
- & - & - & - & - & - \\
- & - & - & - & - & -
\end{array}\right]
\begin{array}{c} p_{1x} \\ p_{1y} \\ p_{1z} \\ p_{2x} \\ p_{2y} \\ p_{2z} \end{array}
\end{array}
$$

As it was already pointed out in the previous paragraph, 6 variables (2 times 3 components of the momentum vectors of the two protons) have been measured in the experiment. It was assumed in the analysis, that an event with the missing mass equal to the mass of the η' meson (within the experimental resolution) corresponds to the $pp \to pp\eta'$ reaction. Under this assumption only five of the kinematical variables are independent compared to six measured variables. Therefore, a kinematical fitting procedure can be applied to improve the effect of the limiting resolution. Hence, the protons momenta were varied demanding that the missing mass of the unregistered particle is exactly equal to the known mass of the η' meson and there has been chosen the momentum vector which was the closest to the vector determined from the experiment. The inverse of the covariance matrix was used as a metric for the distance calculation. The kinematical fit clearly improves the effective resolution, what can be seen in figure 9.1.

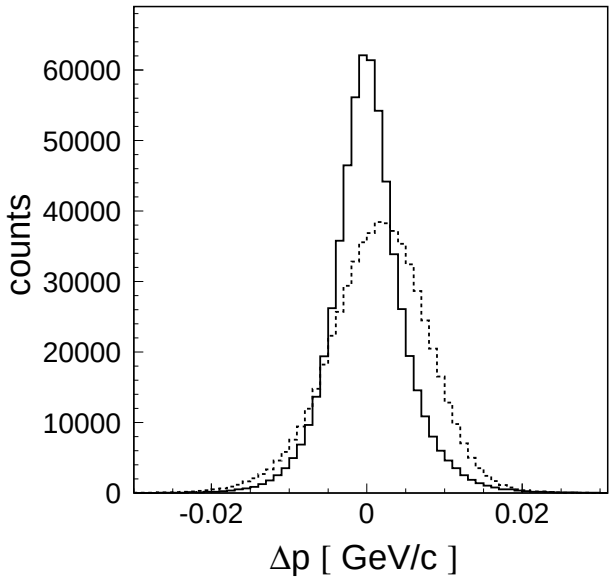

Figure 9.1: Spectrum of the difference between the simulated and reconstructed proton momentum. The dashed line denotes the spectrum before kinematical fit and the solid line corresponds to the situation after the fitting procedure.

After the kinematical fit was performed for each event aside from the experimentally determined momentum vector: $P^{exp} = [p_{1x}^{exp}, p_{1y}^{exp}, p_{1z}^{exp}, p_{2x}^{exp}, p_{2y}^{exp}, p_{2z}^{exp}]$,
the kinematically fitted momenta: $P^{fit} = [p_{1x}^{fit}, p_{1y}^{fit}, p_{1z}^{fit}, p_{2x}^{fit}, p_{2y}^{fit}, p_{2z}^{fit}]$ were obtained.
The P^{fit} vectors are more precise and assure that the determined distributions do not spread beyond the kinematical boundaries.
For the further analysis of events corresponding to the η' production, the distribution of the χ^2 from the kinematical fit procedure was checked. In figure 9.2 the χ^2 distribution as a function of the missing mass determined for the experimental momentum vectors is presented. Having each event described by the two vectors P^{exp} and P^{fit} and the χ^2 of the kinematical fit, the variables s_{pp}, $s_{p\eta'}$, ψ and $|cos\theta^*_{\eta'}|$ were evaluated by using the kinematically fitted vectors P^{fit} if the χ^2–value of the fit for the event was lower than 1.5. However, if the χ^2 was larger than this limitation, P^{exp} were used, since those events correspond to the background with a missing mass lower or higher than the η' meson mass. For the multi-pion production background the kinematical fit procedure is not justified.

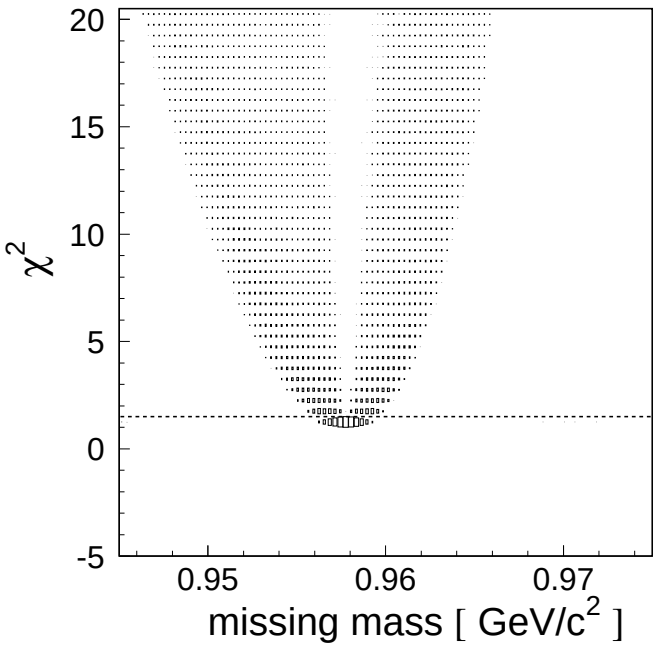

Figure 9.2: The χ^2 distribution as a function of the missing mass. The dashed line at $\chi^2 = 1.5$ visualizes the cut used in the analysis for the separation between kinematically fitted events (P^{fit}) and events without the fit (P^{exp}).

The evaluation of the differential distributions requires only events corresponding to the $pp \to pp\eta'$ reaction. In order to select the number of those events from the multi-pion production reactions, a missing mass spectrum for each studied interval of the variables: s_{pp}, $s_{p\eta'}$, ψ and $|cos\theta^*_{\eta'}|$ was determined. In the next section, the procedure of the background

subtraction applied in the analysis will be discussed.

9.2 Background subtraction

In the following section the method of the multi-pion background subtraction is presented as used in the analysis.
For the background free determination of the differential s_{pp}, $s_{p\eta'}$, ψ and $|cos\theta^*_{\eta'}|$ distributions, first the distribution of the considered variable has been divided into a reasonable number of bins, and then for each bin a missing mass spectrum was produced and the number of the $pp \to pp\eta'$ events was calculated for each interval of s_{pp}, $s_{p\eta'}$, ψ and $|cos\theta^*_{\eta'}|$ separately.
The missing mass distributions include a smooth multi-pion production below and above the produced η' meson mass which allows to estimate the background corresponding to the multi-pion creation in the range of the η' meson signal using a polynomial fitting function, as it was already shown in section 5.2. In figure 9.3, examples of missing mass spectra for two intervals of the invariant proton-proton mass s_{pp} are presented.

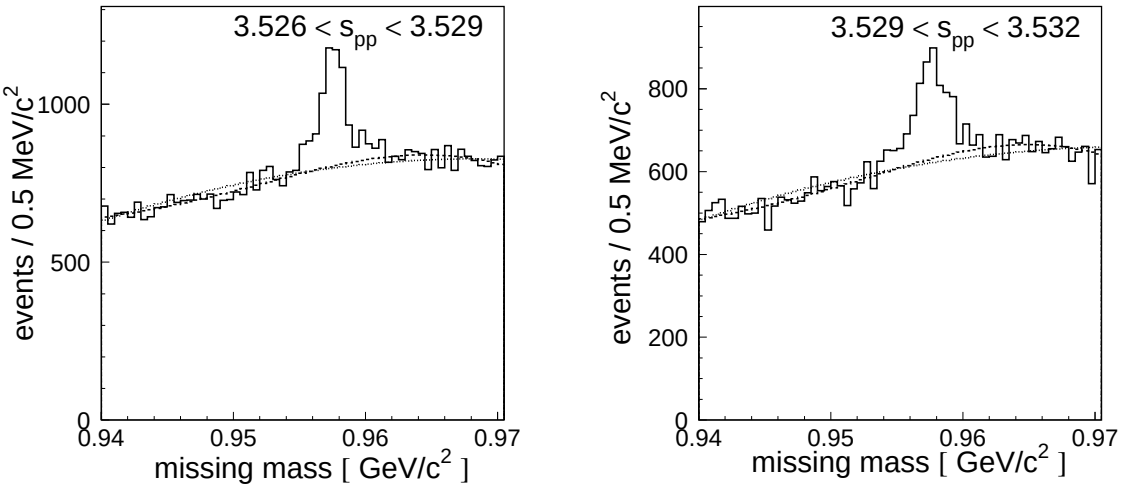

Figure 9.3: Examples of experimental missing mass spectra for two chosen intervals of s_{pp}. The dotted lines indicate the second order polynomial according to the formula 9.2 whereas the dashed lines show the result of the fit of two Gaussian distributions described by the formula 9.3.

In both panels of figure 9.3 the dotted lines correspond to the polynomial fits described by the mathematical function:

$$P(mm, a, b, c) \;=\; a + b \cdot mm \;+\; c \cdot mm^2, \tag{9.2}$$

where mm denotes the missing mass and a, b and c are the free parameters varied during the fit. Since not only a second order polynomial can be used as a good approximation of

the background also a fit by the sum of two Gaussian distributions was performed. The dashed lines in both panels of figure 9.3 correspond to the fit with the function G described by the following formula:

$$G(mm, A_1, B_1, C_1, A_2, B_2, C_2) \;=\; G_1\,(mm, A_1, B_1, C_1) \;+\; G_2\,(mm, A_2, B_2, C_2), \quad (9.3)$$

where the terms G_1 and G_2 denote Gaussian distributions depending on the parameters A_1, B_1, C_1, A_2, B_2 and C_2 varied freely during the fit and mm stands for the missing mass. The fits were performed using the functions of the missing mass (9.2 and 9.3) in the whole range of missing mass outside of the $pp \to pp\eta'$ signal. As it is seen, the fitted functions reproduce the background very well.

The smooth behaviour of the multi-pion background was verified by Monte Carlo simulations. But in order to use these Monte Carlo distributions as a reasonable description for the background an extensive time consuming simulation studies would be necessary. Therefore, a smooth function adjusted to the regions beside the η' peak was used instead. The sum of two Gaussian distributions was applied in the analysis. It should be stressed that the alternative description with the second order polynomial is in rather good agreement with the result obtained using formula 9.3.

The situation is more complicated for missing mass spectra with the signal close to the kinematical limit (see e.g. Fig. 9.4). In this case the shape of the background on the right side of the peak cannot be easily predicted. Such spectra are obtained for kinematical regions of higher squared invariant proton-proton masses s_{pp} and relatively low squared invariant proton-η' masses $s_{p\eta'}$. In order to describe the shape of the background in those regions, the $pp \to pp2\pi\eta$, $pp \to pp3\pi$ and $pp \to pp4\pi$ reactions[1] have been simulated and the simulated events were analysed in the same way as it was done for the experimental data. The result of these simulations is compared to the experimental data in figure 9.4. The simulations of the different reactions channels were performed with phase space distribution including the proton-proton final state interaction [22, 60].
The simulated missing mass spectra were fitted to the data using the formula:

$$S(mm, \alpha, \beta, \gamma) \;=\; \alpha \cdot f_{pp\to pp2\pi\eta}(mm) \;+\; \beta \cdot f_{pp\to pp3\pi}(mm) \;+\; \gamma \cdot f_{pp\to pp4\pi}(mm), \quad (9.4)$$

where α, β and γ denote the free parameters varied during the fit procedure. The functions $f_{pp\to pp2\pi\eta}$, $f_{pp\to pp3\pi}$ and $f_{pp\to pp4\pi}$ correspond to the simulated missing mass distributions for the $pp \to pp2\pi\eta$, $pp \to pp3\pi$ and $pp \to pp4\pi$ reactions.

[1] Those background reaction channels were chosen as a representation of possible multi-pion production background. Since, the $pp \to pp5\pi$ and $pp \to pp6\pi$ reactions simulations can be neglected and the $pp \to pp2\pi$ missing mass of two protons spectrum has similar shape as those for 3π and 4π [71], only simulations for listed reactions were performed.

In figure 9.4, examples of missing mass spectra for squared invariant proton-proton masses $s_{pp} \in [3.577;\ 3.580]$ GeV^2/c^4 (left panel) and squared invariant proton-η' masses $s_{p\eta'} \in [3.602;\ 3.605]$ GeV^2/c^4 (right panel) are presented.

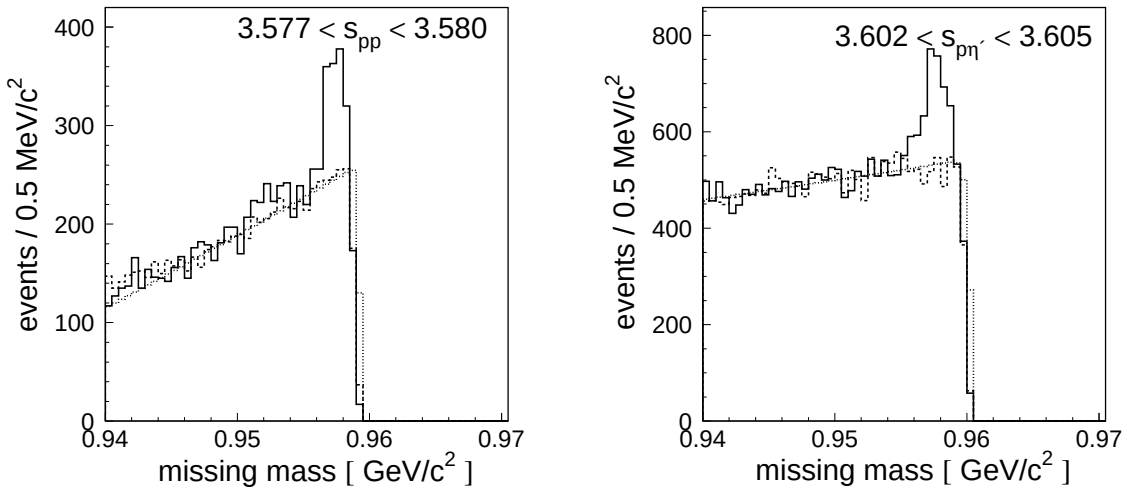

Figure 9.4: Examples of missing mass spectra determined experimentally for the $pp \to ppX$ reaction (solid lines) with superimposed Monte-Carlo simulations (dashed lines) including $pp \to pp2\pi\eta$, $pp \to pp3\pi$ and $pp \to pp4\pi$ reactions, fitted in amplitude to the experimental data. Missing mass spectra for squared invariant proton-proton mass $s_{pp} \in [3.577;\ 3.580]$ GeV^2/c^4 (left panel) and squared invariant proton-η' mass $s_{p\eta'} \in [3.602;\ 3.605]$ GeV^2/c^4 (right panel). The dotted lines in both panels correspond to the fit of the formula 9.5.

In both examples, it is clearly seen that the simulations are in a good agreement with the experimental background distributions below the η' peak. Moreover the behaviour of the simulated background fits well to the kinematical limit of the missing mass distributions. Close to the kinematical boundary, the interaction in the final state is dominated by the proton-proton interaction [60] and this interaction influences strongly the shape of the observed missing mass spectra. Therefore, it was taken into account in the calculations according to the formulas of reference [22] presented in details in appendix B.
For the dynamics of the pion production it had been assumed, that pions are produced homogeneously over the phase space. As it was described in reference [60], the shape of the missing mass spectrum does not change significantly at the edge of the kinematical limit if one assumes resonant or direct pion production.
In order to raise the confidence to the estimation of the background behaviour near the kinematical boundary, those distributions were described in an independent way with a second order polynomial divided by the Fermi function for the description of the rapid

slope at the end of the distributions. To this end the following formula was applied:

$$F(mm, a, b, c, d, g) \;=\; (a \;+\; b \cdot mm \;+\; c \cdot mm^2)/(1 \;+\; e^{(mm \;-\; d)/g}), \qquad (9.5)$$

where a, b, c, d and g are the free parameters varied during the fit procedure.
The results are presented in figure 9.4 as dotted lines. It is seen that under the η' peak the result of formula 9.5 agrees well with the background determined from the simulations and that both reproduce the shape of the slope quite well.

In order to perform a further check of the background estimation, examples of the missing mass distributions for the regions of the squared invariant masses of proton-proton and proton-meson where the η' is not produced are presented. The missing mass distributions are shown in figure 9.5 and represent the regions of low squared invariant masses of the proton-meson subsystem (left) and high squared invariant masses of the proton-proton subsystem (right). For such values of s_{pp} or $s_{p\eta'}$ the production of the η' meson is not possible because $s_{p\eta'} < (m_p + m_{\eta'})^2$ and s_{pp} is too large leaving not enough energy for the η' meson creation.
The fitted simulations reproduce the background very well.

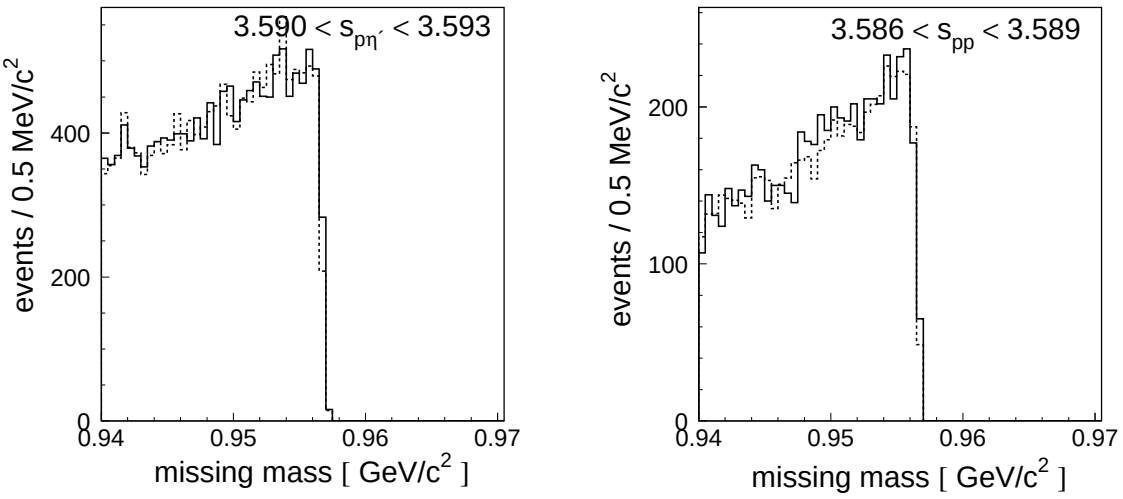

Figure 9.5: Missing mass spectra for low values of $s_{p\eta'} \in [3.590;\ 3.593]$ GeV^2/c^4 (left) and high values of $s_{pp} \in [3.586;\ 3.589]$ GeV^2/c^4 (right). The dashed lines correspond to the simulations of the $pp \to pp2\pi\eta$, $pp \to pp3\pi$ and $pp \to pp4\pi$ reactions fitted to the experimental distributions (solid lines) using only the amplitudes as free parameters.

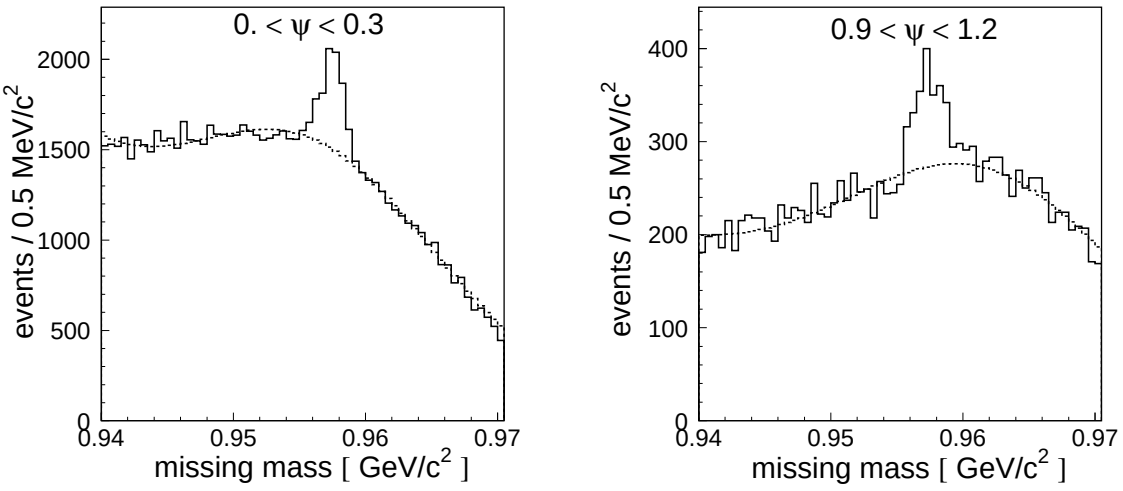

Figure 9.6: Examples of missing mass spectra determined for the first and fourth bin of the ψ angle with a width of 0.3 *radian*. The dashed lines correspond to fits using the function described by formula 9.3.

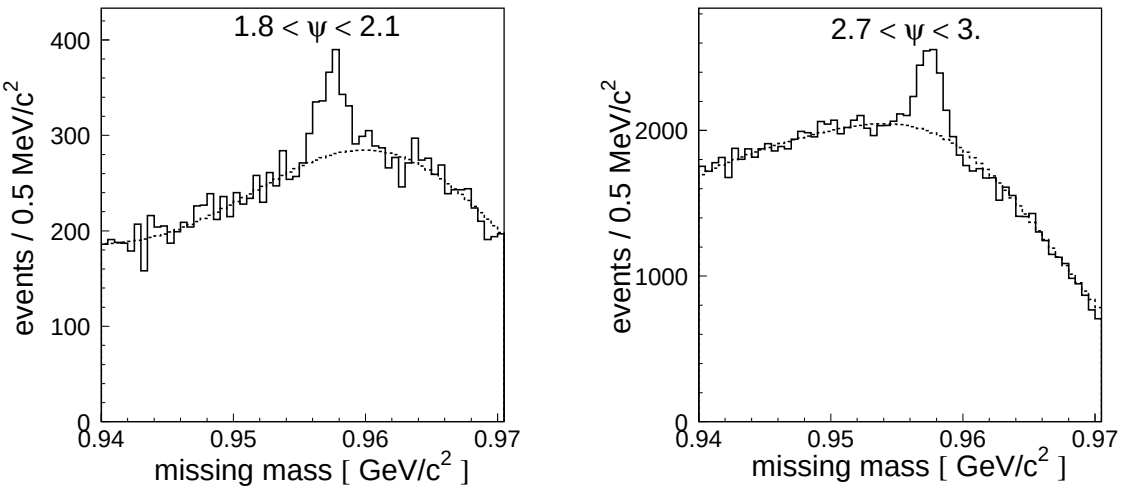

Figure 9.7: Examples of missing mass spectra determined for the seventh and tenth bin of the ψ angle with a width of 0.3 *radian*. The dashed lines correspond to fits employing the function described by formula 9.3.

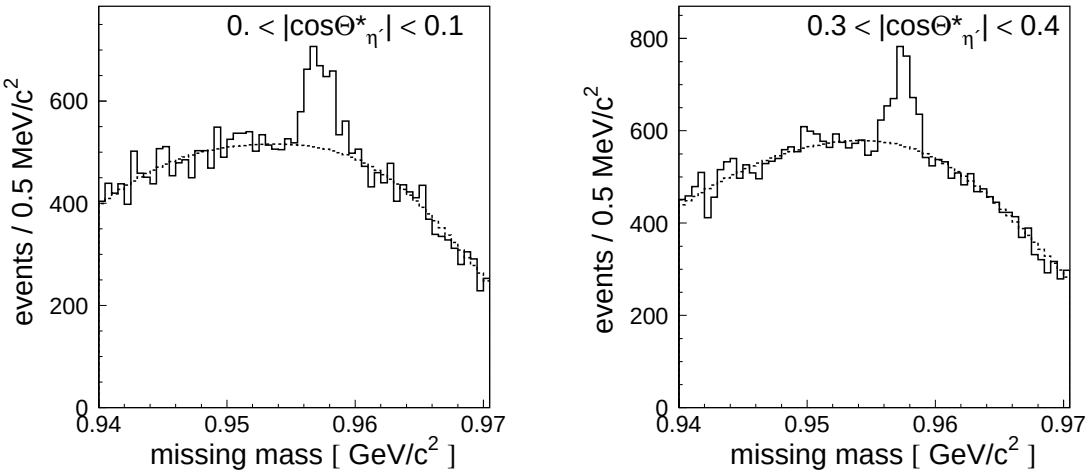

Figure 9.8: Examples of missing mass spectra determined for the first and fourth bin of $|cos\theta^*_{\eta'}|$ with a width corresponding to $\Delta|cos\theta^*_{\eta'}| = 0.1$. The dashed lines correspond to fits according to the function described by formula 9.3.

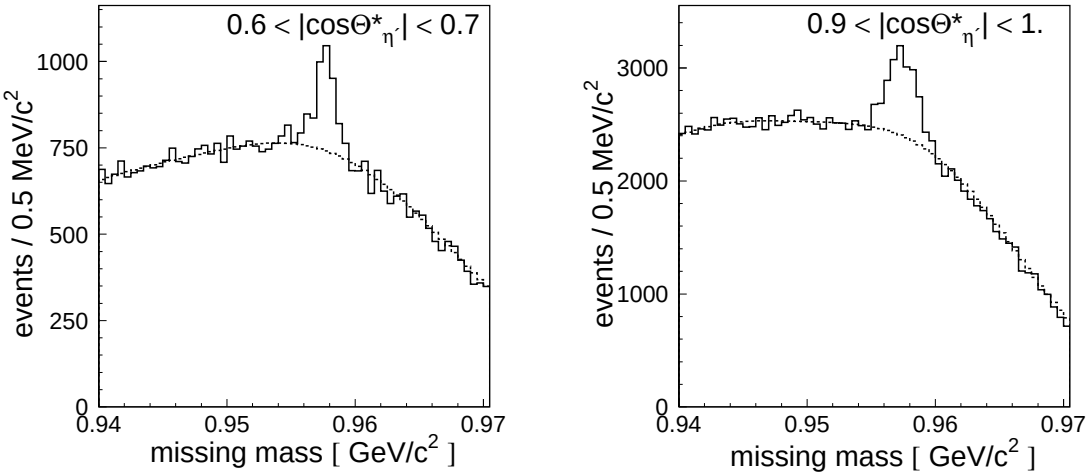

Figure 9.9: Examples of missing mass spectra determined for the seventh and tenth bin of $|cos\theta^*_{\eta'}|$ with a width corresponding to $\Delta|cos\theta^*_{\eta'}| = 0.1$. The dashed lines correspond to fits using the function as described by formula 9.3.

In case of the angular distributions the background could be described as a polynomial or Gaussian in the whole angular range. This is because the signal from the η' meson is far from the kinematical limit for all spectra (see Fig. 9.6, 9.7, 9.8 and 9.9) and additionally the background varies smoothly on both sides of the peak. In this context it is also important

to note that the width of the peak is due to the experimental resolution and since the background is smooth on both sides, no structures are being expected below the peak as it is verified by the simulation studies including relevant background channels.
Missing mass distributions for every third bin of ψ and $|cos\theta^*_{\eta'}|$ are presnted in figures 9.6, 9.7, 9.8 and 9.9, respectively, using formula 9.3 for fitting to the background.

9.3 Systematic errors of background estimation

The main contribution of the systematic uncertainty of the differential cross section determination comes from the uncertainty of the estimation of the yield of the η' events which in turn is due to the assumption of the shape of the background. In order to estimate those errors, the numbers of background events extracted under two different assumptions were compared. For the missing mass spectra with the signal far from the kinematical limit the background determined by Gaussian distributions with the background estimated by a second order polynomial were compared. Whereas, for the spectra close to the kinematical limit a comparison of the background determination by Monte-Carlo simulations with a second order polynomial divided by the Fermi distribution was performed. The relative difference between determined numbers of events N^A_{back} (two Gaussian distributions or Monte-Carlo simulations fit, respectively) and N^B_{back} (polynomial fit) was used as an estimation for the systematic uncertainty of the differential cross sections evaluation.
The relative systematic errors, expressed in per cent were calculated in the following way:

$$\Delta_{back} = \frac{N^A_{back} - N^B_{back}}{N^A_{back} + N^B_{back}} \cdot 100\%. \tag{9.6}$$

The averaged value of the systematic deviations in the various applied fit procedures calculated according to formula 9.6 are below 3%.
The systematic uncertainty of the differential cross sections evaluation was calculated using the formula:

$$\Delta_{sys}\Big(\frac{d\sigma}{df}(f)\Big) = \frac{d\sigma}{df}(f) \cdot \frac{N_{back}(f)}{N_{\eta'}(f)} \cdot 0.03, \tag{9.7}$$

where f stands for both the squared invariant proton-proton mass s_{pp} and the squared invariant proton-η' mass $s_{p\eta'}$. N_{back} and $N_{\eta'}$ correspond to the average numbers of background and η' creation events, respectively. The averaged values of the systematic errors for the differential cross sections, calculated according to formula 9.7, are in the order of 0.32 $\mu b/(\mathrm{GeV}^2/\mathrm{c}^4)$ and will be presented in details in the next chapter.

10. Cross sections

This chapter is devoted to the derivation of the final results.

10.1 Acceptance corrections

The COSY-11 detector setup does not cover the full 4π solid angle in the centre-of-mass system of the $pp \to pp\eta'$ reaction at the proton beam momentum of $P_B = 3.260$ GeV/c. Therefore, in order to study the differential cross sections, one has to perform acceptance corrections for the measured distributions.
In general, the acceptance corrections should be done in the five dimensional phase space of e.g. s_{pp}, $s_{p\eta'}$, ϕ, ψ and $cos\theta^*_{\eta'}$ (as depicted in chapter 2.3).
But one can safely assume that the dependence on the $\phi^*_{\eta'}$ angle, the centre-of-mass azimuthal angle of the η' meson momentum, is isotropic because of the axial symmetry of the initial unpolarized state. In addition, the identical particles in the initial state imply that the distribution of $cos\theta^*_{\eta'}$ should be symmetrical around 90^o. This limits the variables for the differential acceptance to s_{pp}, $s_{p\eta'}$, ψ and $|cos\theta^*_{\eta'}|$.
To determine the distributions of squared invariant masses s_{pp} and $s_{p\eta'}$, the available range was divided into 22 bins. Number and width of the bins were chosen as a compromise between statistics and the experimental resolution. The width of the bins was chosen for the variables s_{pp} and $s_{p\eta'}$ to be 0.003 GeV^2/c^4.
In the case of angular distributions, the $|cos\theta^*_{\eta'}|$ range was divided into 10 bins with a bin width of 0.1, and the ψ range into 11 bins of 0.3 radian.
The acceptance correction of the data will be performed iteratively. First, it was assumed that the distributions are determined by a homogeneous phase space occupation modulated by the pp-FSI. Under this assumption the acceptance was calculated and the differential cross section for the variables s_{pp}, $s_{p\eta'}$, ψ and $|cos\theta^*_{\eta'}|$ was extracted. Next, using the derived distributions the acceptance was calculated and the whole procedure was repeated until the differential distributions remain unaltered.
In order to calculate the differential acceptance it was assumed that the distribution over the ψ angle is isotropic like it was experimentally determined for the $pp \to pp\rho$, $pp \to pp\omega$ and $pp \to pp\phi$ reactions [76,77].
The geometrical acceptance as a function of s_{pp} and $s_{p\eta'}$ is presented in the left and right panel of figure 10.1, respectively. In figure 10.2, the acceptance dependence for the $|cos\theta^*_{\eta'}|$ and the ψ angular distributions is shown.

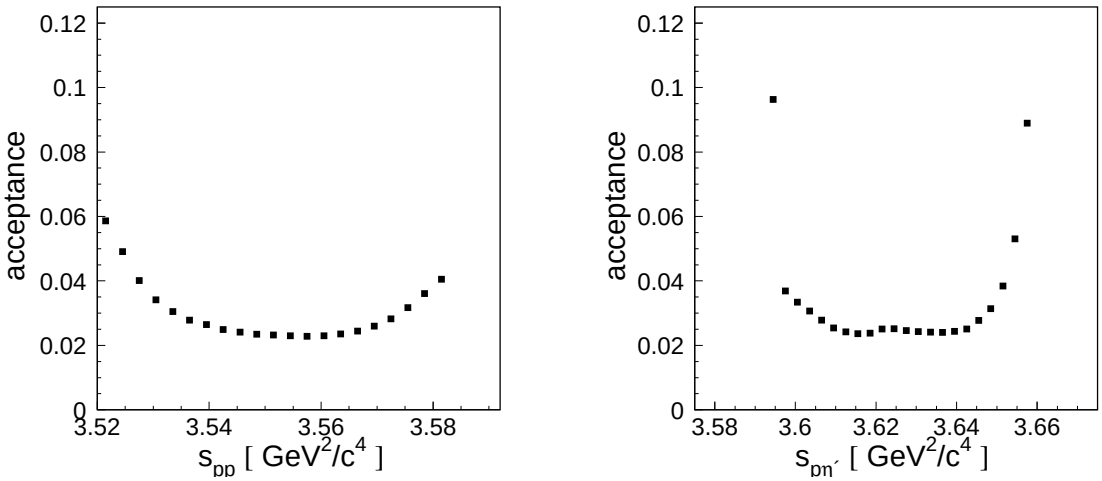

Figure 10.1: Geometrical acceptance of the COSY-11 detection setup determined for the $pp \to pp\eta'$ reaction, simulated for a beam momentum $P_B = 3.260$ GeV/c, as a function of the squared invariant mass of the proton-proton subsystem (left), and the squared invariant mass of the proton-η' subsystem (right).

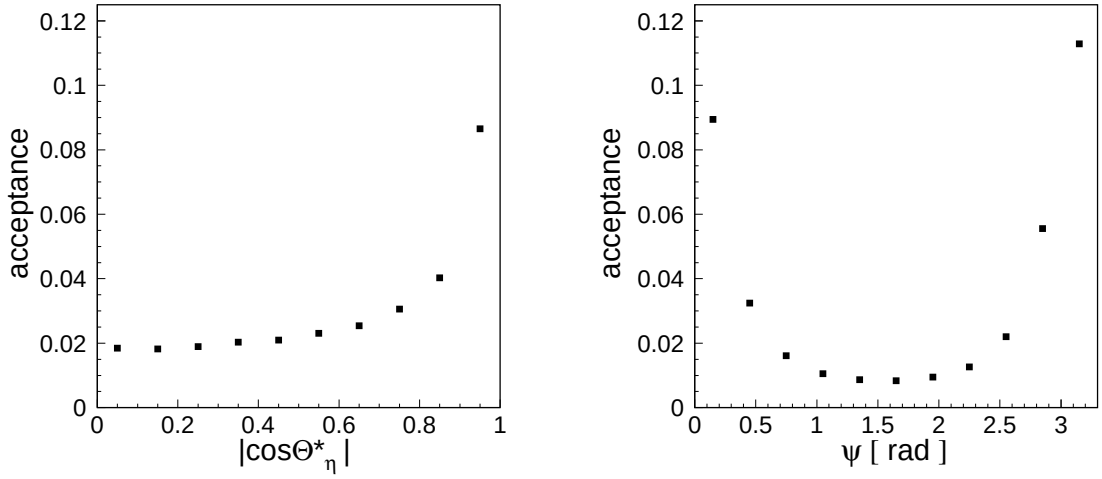

Figure 10.2: The COSY-11 detection acceptance as a function of the polar angle of the η' meson momentum vector $|cos\theta^*_{\eta'}|$ (left), and for the ψ angle describing the rotation of the reaction plane around the direction of the η' meson momentum (right).

After performing the luminosity determination and having calculated the geometrical acceptance, one can evaluate angular distributions. In figure 10.3 the differential distri-

bution of the cosine of the $\theta^*_{\eta'}$ polar angle is presented. The distribution has an isotropic character within the statistical errors.

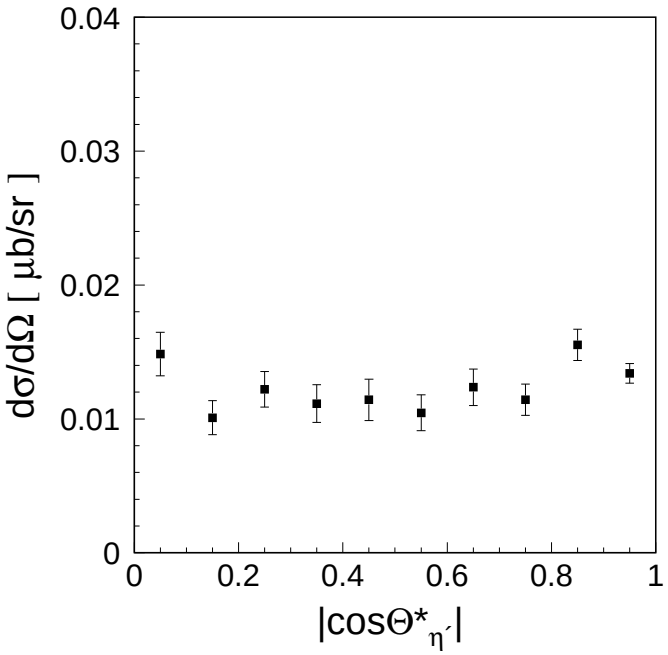

Figure 10.3: Distribution of $|cos\theta^*_{\eta'}|$ of the η' meson momentum vector in the centre-of-mass frame. The shown result was evaluated under the assumption that $\frac{d\sigma}{d\psi}$ is isotropic.

Then, the angular distribution of the ψ angle was calculated. Unexpectedly, but similar to the situation observed for such a distribution for the $pp \to pp\eta$ reaction [9] measured at the excess energy of 15.5 MeV, a significant anisotropic behaviour of the ψ angle distribution is observed. The $\frac{d\sigma}{d\psi}$ distribution determined experimentally is presented in figure 10.4. Such a shape cannot be explained by any background behaviour since $\frac{d\sigma}{d\psi}$ was extracted for each bin separately, as it was mentioned earlier in section 9.2, and in fact the distribution shown in figure 10.4 is background-free. Systematic errors in the background subtraction are expected to be much smaller and can also not cause such an anisotropy. The missing mass spectra used for the background subtraction could satisfactorily well be reproduced for each bin in the phase space. For example see figures 9.6 and 9.7 in section 9.2.
Due to the anisotropic behaviour of the $\frac{d\sigma}{d\psi}$ the full procedure of acceptance correction for the $|cos\theta^*_{\eta'}|$, s_{pp} and $s_{p\eta'}$ distributions was performed once again with the working assumption that the distribution $\frac{d\sigma}{d\psi}$ is as it was determined from the data. The procedure was repeated three times. After all, it was observed that the output distributions are in good agreement with the input values.
It was also checked that the shape of the ψ distribution assumed in the calculations of the acceptance does not influence the shape of s_{pp}, $s_{p\eta'}$ and $|cos\theta^*_{\eta'}|$ distributions.

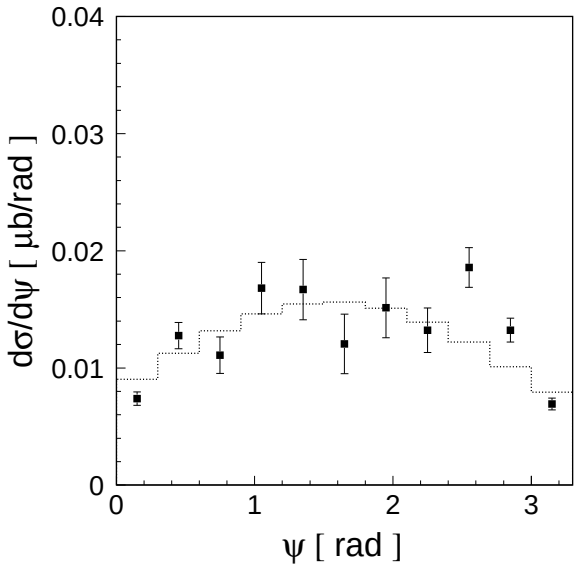

Figure 10.4: Distribution of the differential cross section as a function of the ψ angle determined experimentally. The superimposed histogram corresponds to a fit by the function $y = a + b \cdot |sin(\psi)|$, where $a = 7.87$ nb/rad and $b = 7.77$ nb/rad. Since, in the analysis the advantage of the symmetry $\frac{d\sigma}{d\psi}(\psi) = \frac{d\sigma}{d\psi}(\psi + \pi)$ was taken, only the range of ψ from 0 to π is presented.

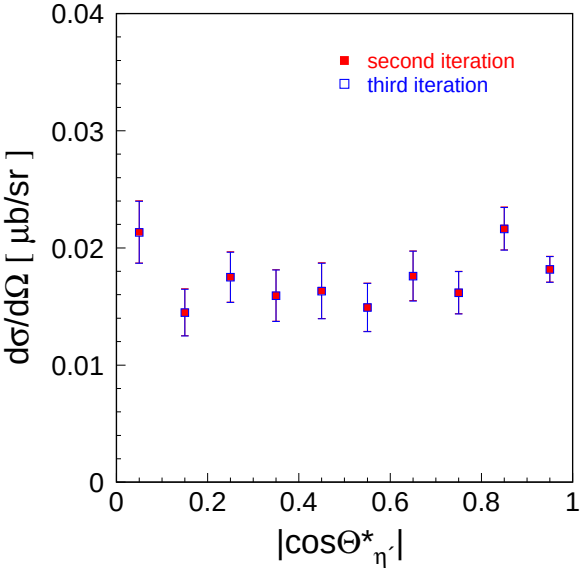

Figure 10.5: Distribution of the $|cos\theta^*_{\eta'}|$ of the η' meson momentum vector in the centre-of-mass frame. The distributions after the second (closed squares) and third (open squares) iterations are compared (for details see text). The distributions are nearly identical and therefore the points can be hardly distinguished.

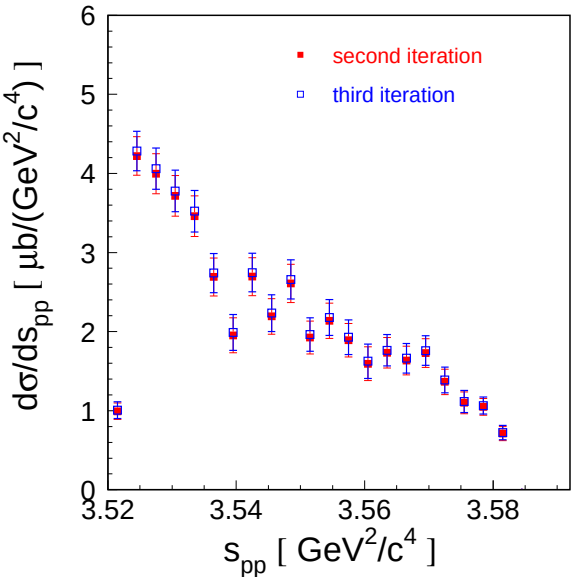

Figure 10.6: Comparison of the invariant mass s_{pp} distributions after the second (showed as closed squares) and third (presented as open squares) iterations assuming different assumption about the ψ distribution.

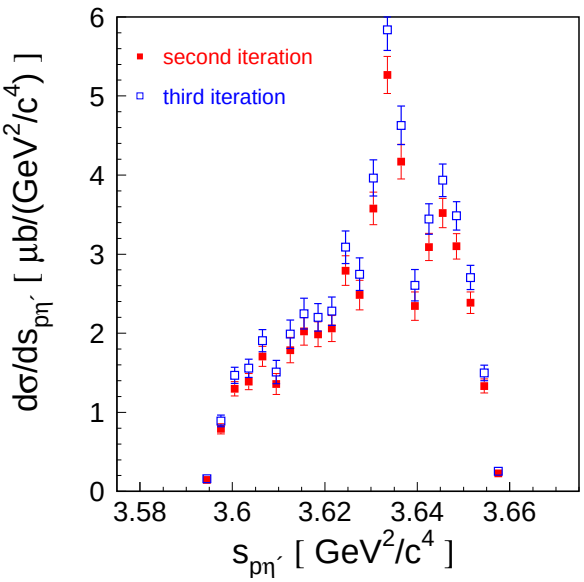

Figure 10.7: Comparison of the invariant mass $s_{p\eta'}$ distributions after the second (showed as closed squares) and third (presented as open squares) iterations assuming different assumption about the ψ distribution.

As an example figure 10.5 presents the $|cos\theta^*_{\eta'}|$ spectrum determined assuming a ψ distribution obtained from the second and the third iteration.
Similarly like in case of the distribution of the cross section as a function of $|cos\theta^*_{\eta'}|$, the differential cross sections as a function of s_{pp} and $s_{p\eta'}$ were extracted. First, as it was mentioned, the distributions were determined with the assumption of an isotropic behaviour of the angular distributions of polar and azimuthal angle of the η' meson momentum vector in the centre-of-mass frame, and also an isotropic behaviour of the ψ angle distribution.

Then, again using the experimental parameterization of the distribution of the cross section as a function of the ψ angle in the centre-of-mass frame, the invariant mass s_{pp} and $s_{p\eta'}$ distributions were determined. Results of the second and third iterations are shown in figures 10.6 and 10.7.
Again, it can be observed that the shapes of the distributions after the second and third iterations are in agreement.

10.2 Total and differential cross sections

In this section, the results of the total cross section and differential cross sections determined for the $pp \to pp\eta'$ reaction are presented.

The total cross section for the $pp \to pp\eta'$ reaction, determined at an excess energy of Q = 16.4 MeV, is presented in figure 10.8 and amounts to: 139 $\pm$3 nb. In the calculations the final distribution of the s_{pp}, $s_{p\eta'}$, ψ and $|cos\theta^*_{\eta'}|$ were taken into account.
Though, the shapes of distributions s_{pp}, $s_{p\eta'}$ and $|cos\theta^*_{\eta'}|$ are independent of the ψ distribution, the total cross section depends quite significantly on the shape of $\frac{d\sigma}{d\psi}$ [9] which is assumed for the acceptance calculations. The obtained value agrees within the errors to the previously determined cross section values, however, it is slightly higher than the former data. This is due to the fact that in the previous analyses [25–27] the acceptance was calculated only approximately disregarding the differential distributions of the ψ angle which was not established due to lack of statistics. A similar effect of an increase in the cross section values after taking into account the differential distribution of ψ was obtained in the case of the η meson [9].
The systematic error of the total cross section contains a systematic error of the luminosity determination which amounts to 3% as it was evaluated in [1] and the uncertainty from the $\frac{d\sigma}{d\psi}$ distribution, since varying the parameters of the function $\frac{d\sigma}{d\psi} = a + b \cdot |sin(\psi)|$ (within their uncertainties), they change the total cross section by 2.5 nb. The averaged systematic error of the background subtraction (like pointed out in section 9.3) amounts to 5 nb.

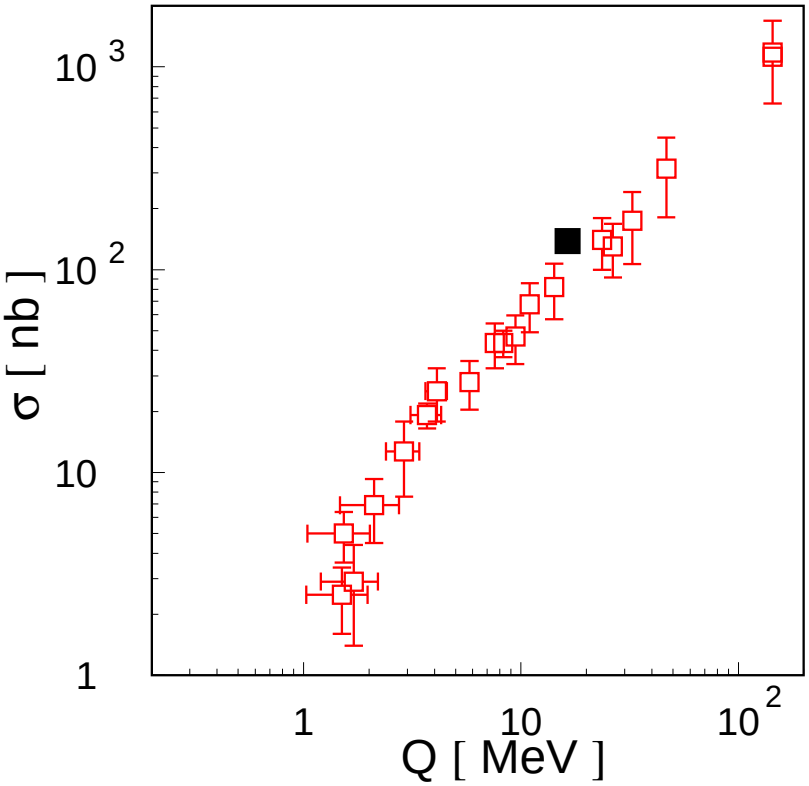

Figure 10.8: Excitation function for the $pp \rightarrow pp\eta'$ reaction. The earlier measurements [23–28] are presented as open squares, the closed black square depicts the total cross section determined for the excess energy Q = 16.4 MeV (the result of this thesis). The error bars denote the total uncertainty (statistical and systematic).

Thus, the systematic error of the total cross section adds up to 12 nb. Summarizing, the total cross section for the $pp \rightarrow pp\eta'$ reaction determined at the excess energy of 16.4 MeV is equal to $\sigma = (\mathbf{139\ \pm 3\ \pm 12})$ **nb** where the indicated errors are statistical and systematic, respectively.

In the following tables and figures, the values of the differential cross sections as functions of the observables $|cos\theta^*_{\eta'}|$, ψ, s_{pp}, and $s_{p\eta'}$ defined earlier in section 2.3 are presented. In all tables and figures statistical and systematic errors are included.
The distribution of the polar angle is listed in table 10.1 and presented in figure 10.9.
The distribution of the ψ angle is listed in table 10.2 and presented in figure 10.10.
In tables 10.3 and 10.4, the results for the differential cross sections of the invariant masses pp and $p\eta'$ are presented, respectively. The listed values of both distributions are shown in figure 10.11.

$\lvert cos\theta^*_{\eta'}\rvert$	$\frac{d\sigma}{d\Omega}(\lvert cos\theta^*_{\eta'}\rvert)$ $[\mu b/sr]$
0.05	$0.0270 \pm 0.0034_{stat} \pm 0.0045_{sys}$
0.15	$0.0184 \pm 0.0025_{stat} \pm 0.0026_{sys}$
0.25	$0.0222 \pm 0.0027_{stat} \pm 0.0029_{sys}$
0.35	$0.0202 \pm 0.0028_{stat} \pm 0.0037_{sys}$
0.45	$0.0207 \pm 0.0030_{stat} \pm 0.0046_{sys}$
0.55	$0.0189 \pm 0.0026_{stat} \pm 0.0038_{sys}$
0.65	$0.0223 \pm 0.0027_{stat} \pm 0.0043_{sys}$
0.75	$0.0205 \pm 0.0023_{stat} \pm 0.0038_{sys}$
0.85	$0.0274 \pm 0.0023_{stat} \pm 0.0048_{sys}$
0.95	$0.0230 \pm 0.0014_{stat} \pm 0.0039_{sys}$

Table 10.1: The differential cross sections as a function of $\lvert cos\theta^*_{\eta'}\rvert$ for the $pp \to pp\eta'$ reaction measured at Q = 16.4 MeV.

ψ $[rad]$	$\frac{d\sigma}{d\psi}$ $[\mu b/rad]$
0.15	$0.0118 \pm 0.0009_{stat} \pm 0.0023_{sys}$
0.45	$0.0193 \pm 0.0017_{stat} \pm 0.0029_{sys}$
0.75	$0.0177 \pm 0.0025_{stat} \pm 0.0030_{sys}$
1.05	$0.0276 \pm 0.0036_{stat} \pm 0.0040_{sys}$
1.35	$0.0276 \pm 0.0043_{stat} \pm 0.0046_{sys}$
1.65	$0.0200 \pm 0.0042_{stat} \pm 0.0044_{sys}$
1.95	$0.0251 \pm 0.0042_{stat} \pm 0.0050_{sys}$
2.25	$0.0215 \pm 0.0031_{stat} \pm 0.0036_{sys}$
2.55	$0.0286 \pm 0.0026_{stat} \pm 0.0046_{sys}$
2.85	$0.0202 \pm 0.0016_{stat} \pm 0.0042_{sys}$
3.15	$0.0117 \pm 0.0009_{stat} \pm 0.0024_{sys}$

Table 10.2: Differential cross sections as a function of the ψ angle determined for the $pp \to pp\eta'$ reaction measured at Q = 16.4 MeV. Since, $\frac{d\sigma}{d\psi}(\psi) = \frac{d\sigma}{d\psi}(\psi + \pi)$, the full range for ψ angle is assumed from 0 to π.

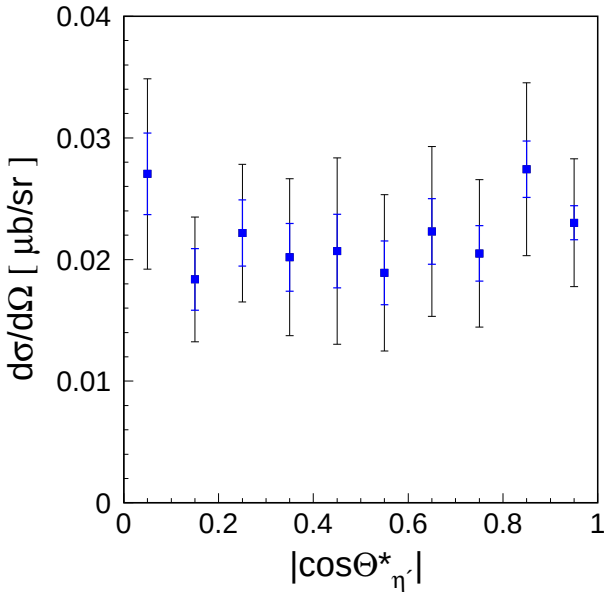

Figure 10.9: Distribution of the polar angle of the η' meson emission in the centre-of-mass system. The error bars represent statistical and total (statistical + systematic) uncertainties.

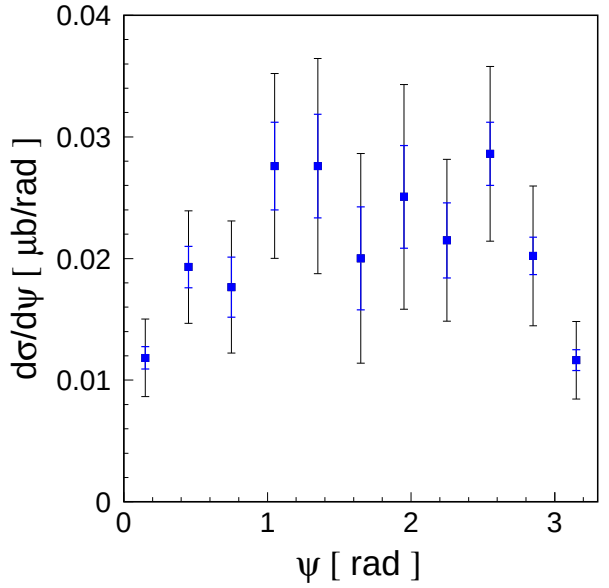

Figure 10.10: Differential cross section as a function of the ψ angle obtained after the last iteration. The error bars represent statistical and total (statistical + systematic) uncertainties.

s_{pp} $[GeV^2/c^4]$	$\frac{d\sigma}{ds_{pp}}$ $[\mu\mathrm{b}/\mathrm{GeV}^2/\mathrm{c}^4]$
3.5215	$1.01 \pm 0.11_{stat} \pm 0.12_{sys}$
3.5245	$4.28 \pm 0.25_{stat} \pm 0.56_{sys}$
3.5275	$4.06 \pm 0.26_{stat} \pm 0.59_{sys}$
3.5305	$3.78 \pm 0.26_{stat} \pm 0.55_{sys}$
3.5335	$3.52 \pm 0.26_{stat} \pm 0.52_{sys}$
3.5365	$2.74 \pm 0.25_{stat} \pm 0.46_{sys}$
3.5395	$1.99 \pm 0.23_{stat} \pm 0.40_{sys}$
3.5425	$2.75 \pm 0.25_{stat} \pm 0.40_{sys}$
3.5455	$2.23 \pm 0.23_{stat} \pm 0.37_{sys}$
3.5485	$2.66 \pm 0.25_{stat} \pm 0.39_{sys}$
3.5515	$1.96 \pm 0.21_{stat} \pm 0.30_{sys}$
3.5545	$2.18 \pm 0.23_{stat} \pm 0.34_{sys}$
3.5575	$1.93 \pm 0.22_{stat} \pm 0.31_{sys}$
3.5605	$1.62 \pm 0.22_{stat} \pm 0.33_{sys}$
3.5635	$1.76 \pm 0.20_{stat} \pm 0.26_{sys}$
3.5665	$1.66 \pm 0.19_{stat} \pm 0.24_{sys}$
3.5695	$1.76 \pm 0.19_{stat} \pm 0.26_{sys}$
3.5725	$1.39 \pm 0.16_{stat} \pm 0.22_{sys}$
3.5755	$1.12 \pm 0.14_{stat} \pm 0.19_{sys}$
3.5785	$1.07 \pm 0.11_{stat} \pm 0.11_{sys}$
3.5815	$0.72 \pm 0.09_{stat} \pm 0.09_{sys}$
3.5845	$0.013 \pm 0.004_{stat} \pm 0.002_{sys}$

Table 10.3: Distribution of the squared invariant mass of the proton-proton system (s_{pp}), determined for the $pp \to pp\eta'$ reaction measured at Q = 16.4 MeV.

$s_{p\eta'}$ $[GeV^2/c^4]$	$\frac{d\sigma}{ds_{p\eta'}}$ $[\mu\mathrm{b}/\mathrm{GeV}^2/\mathrm{c}^4]$
3.5945	$0.14 \pm 0.02_{stat} \pm 0.02_{sys}$
3.5975	$0.76 \pm 0.06_{stat} \pm 0.09_{sys}$
3.6005	$1.25 \pm 0.09_{stat} \pm 0.14_{sys}$
3.6035	$1.32 \pm 0.10_{stat} \pm 0.17_{sys}$
3.6065	$1.62 \pm 0.12_{stat} \pm 0.24_{sys}$
3.6095	$1.28 \pm 0.13_{stat} \pm 0.28_{sys}$
3.6125	$1.69 \pm 0.15_{stat} \pm 0.33_{sys}$
3.6155	$1.91 \pm 0.16_{stat} \pm 0.37_{sys}$
3.6185	$1.87 \pm 0.15_{stat} \pm 0.36_{sys}$
3.6215	$1.94 \pm 0.15_{stat} \pm 0.38_{sys}$
3.6245	$2.62 \pm 0.18_{stat} \pm 0.44_{sys}$
3.6275	$2.33 \pm 0.18_{stat} \pm 0.48_{sys}$
3.6305	$3.37 \pm 0.19_{stat} \pm 0.51_{sys}$
3.6335	$4.96 \pm 0.22_{stat} \pm 0.54_{sys}$
3.6365	$3.93 \pm 0.21_{stat} \pm 0.45_{sys}$
3.6395	$2.21 \pm 0.17_{stat} \pm 0.40_{sys}$
3.6425	$2.93 \pm 0.16_{stat} \pm 0.32_{sys}$
3.6455	$3.34 \pm 0.18_{stat} \pm 0.48_{sys}$
3.6485	$2.96 \pm 0.15_{stat} \pm 0.38_{sys}$
3.6515	$2.30 \pm 0.13_{stat} \pm 0.35_{sys}$
3.6545	$1.27 \pm 0.08_{stat} \pm 0.22_{sys}$
3.6575	$0.22 \pm 0.03_{stat} \pm 0.04_{sys}$

Table 10.4: Distribution of the squared invariant mass of the proton-η' system ($s_{p\eta'}$), determined for the $pp \to pp\eta'$ reaction measured at Q = 16.4 MeV.

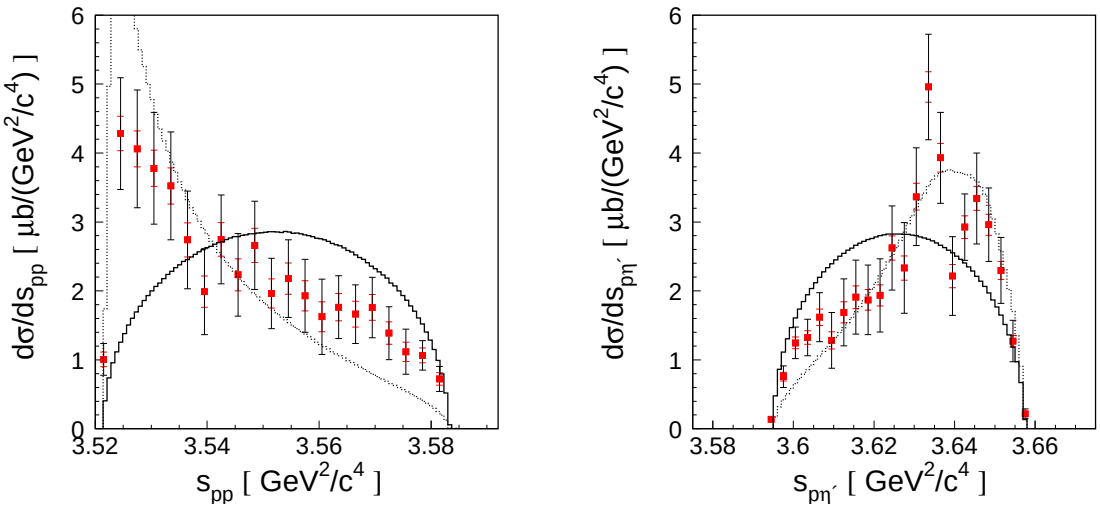

Figure 10.11: Distributions of the squared proton-proton (s_{pp}) and proton-η' ($s_{p\eta'}$) invariant masses, determined experimentally for the $pp \to pp\eta'$ reaction at the excess energy of Q = 16.4 MeV (closed squares). The experimental data are compared to the expectation under the assumption of a homogeneously populated phase space which is presented as solid lines. The integrals of the phase space weighted by the proton-proton scattering amplitude - FSI_{pp} are marked as dotted histograms. The results of the simulations were normalized to the data in amplitude.

In figure 10.11 experimentally determined distributions are compared to the expectation under the assumption of a homogeneously populated phase space, presented in the figure as solid lines. One can see that, for both distributions the data do not agree with the calculations. In the same figure the experimental spectra are compared also to the integrals of the phase space weighted by the proton-proton scattering amplitude - FSI_{pp} which are depicted as dotted histograms. Also the calculations including only the FSI_{pp} do not fit to the data satisfactorily. One can see that the comparison depends on the way of normalization which will be discussed later.

10.3 Comparison with results for the η meson production

The comparison of the distributions of the square of the proton-proton (s_{pp}) and proton-meson ($s_{p-meson}$) invariant masses between the $pp \to pp\eta'$ and the $pp \to pp\eta$ reactions is presented in figure 10.12. For the proton-meson system the comparison was performed for the kinetic energy of the proton-meson system ($\sqrt{s_{p-meson}} - m_p - m_{meson}$) and not as a function of $s_{p-meson}$ because the range of the $s_{p\eta}$ and $s_{p\eta'}$ are different due to the different masses of the η and η' mesons. But the range of ($\sqrt{s_{p-meson}} - m_p - m_{meson}$) is the same since the measurements for the η and η' production were by purpose performed at about

the same excess energy. The differential distributions as a function of s_{pp} are compared directly, because we compare the same system at the same energy range.

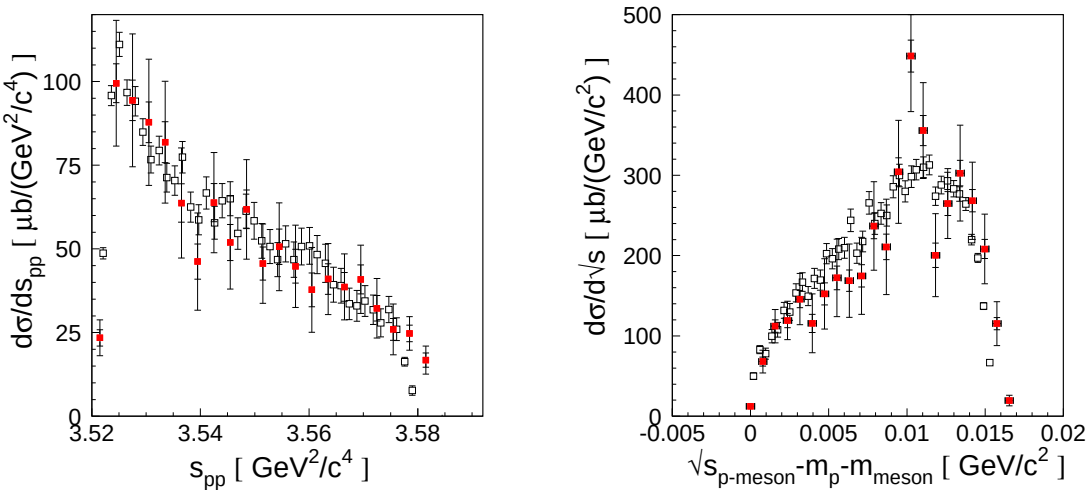

Figure 10.12: The comparison of the distributions of the square of the proton-proton invariant mass (s_{pp}) (left panel) and of proton-meson kinetic energy ($\sqrt{s_{p-meson}} - m_p - m_{meson}$) (right panel). The distributions for the $pp \to pp\eta'$ reaction (closed squares) were normalized to the distributions for the $pp \to pp\eta$ reaction (open squares) with respect to the total cross section.

In both panels it is seen that the experimental points indicating the $pp \to pp\eta$ measurement (open squares) are in agreement with those from the $pp \to pp\eta'$ reaction (closed squares) within the error bars. It is unexpected that the shapes do not differ, showing the same enhancement at the same values of the square of the proton-proton (s_{pp}) invariant mass.

The total cross sections as a function of excess energy for the $pp \to pp\eta$ and $pp \to pp\eta'$ reactions and the comparison of the ratios of the production amplitudes for both reactions and the production amplitude for the $pp \to pp\pi^0$ reaction showed that the interaction within the proton-η should have been stronger than the proton-η' system interaction.

Therefore, if indeed the η'-proton interaction is much smaller than the η-proton as inferred from the excitation function, then the spectra presented here rather exclude the hypothesis that the enhancement (see figures and discussion in section 2.4) is due to the interaction of the meson and the proton. Moreover, based on those distributions it is not possible to disentangle between the hypothesis of the admixture of higher partial waves during the η production or the energy dependence of the production amplitude.

10.4 s_{pp} and $s_{p\eta'}$ distributions in view of theoretical predictions

The interaction should manifest itself in the regions where particles possess small relative velocities as it was mentioned in previous sections.
In figure 10.13 the comparison of the experimentally determined cross sections as a function of the squared invariant mass of the proton-proton system (s_{pp}) to theoretical calculations is presented. One can see the strong deviation of the experimental spectrum from the phase space predictions (solid lines), normalized in amplitude. It can be also seen that the inclusion of the FSI$_{pp}$ [22] improves the agreement but still there is a significant discrepancy between the data and the calculations[1]. Here, it is also presented that two different possible normalizations of the model calculations do not agree with the shape of the experimental distribution. The left panel shows the fit to the lower values of the proton-proton invariant mass. The right one depicts the fitting to the high energy region of s_{pp}.

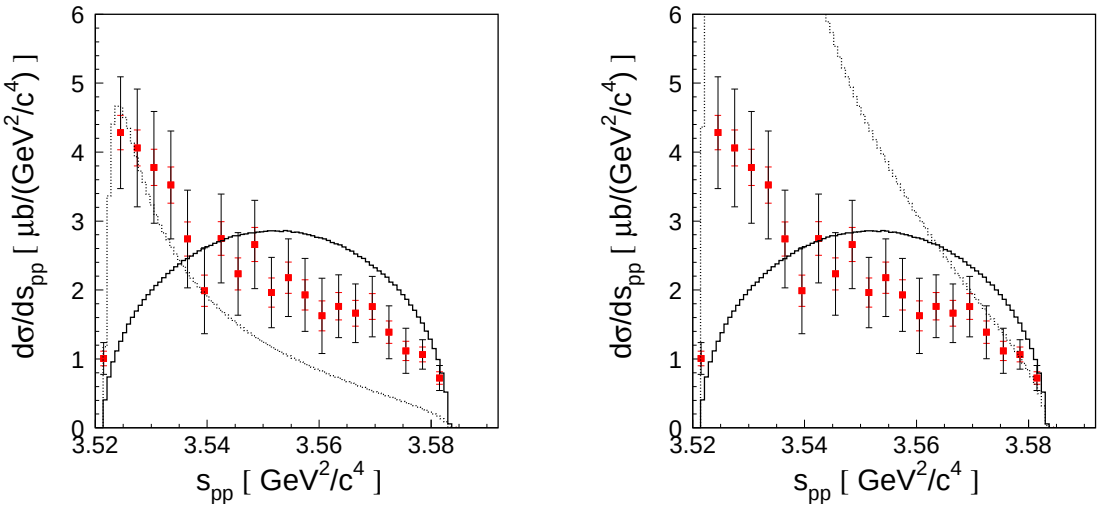

Figure 10.13: Distribution of the square of the proton-proton (s_{pp}) invariant mass determined experimentally for the $pp \to pp\eta'$ reaction (closed squares). The integrals of the phase space weighted by a square of the proton-proton on-shell scattering amplitude (dotted lines)-FSI$_{pp}$ have been normalized arbitrarily to the lower values of s_{pp} in the left panel and to the higher values of s_{pp} in the right panel. The expectations under the assumption of a homogeneously populated phase space are shown as solid lines.

These different normalizations are presented for the invariant mass of the proton-η' subsystem in figure 10.14.

[1] A detailed description of the proton-proton FSI parameterization based on the proton-proton on-shell amplitude is presented in appendix B

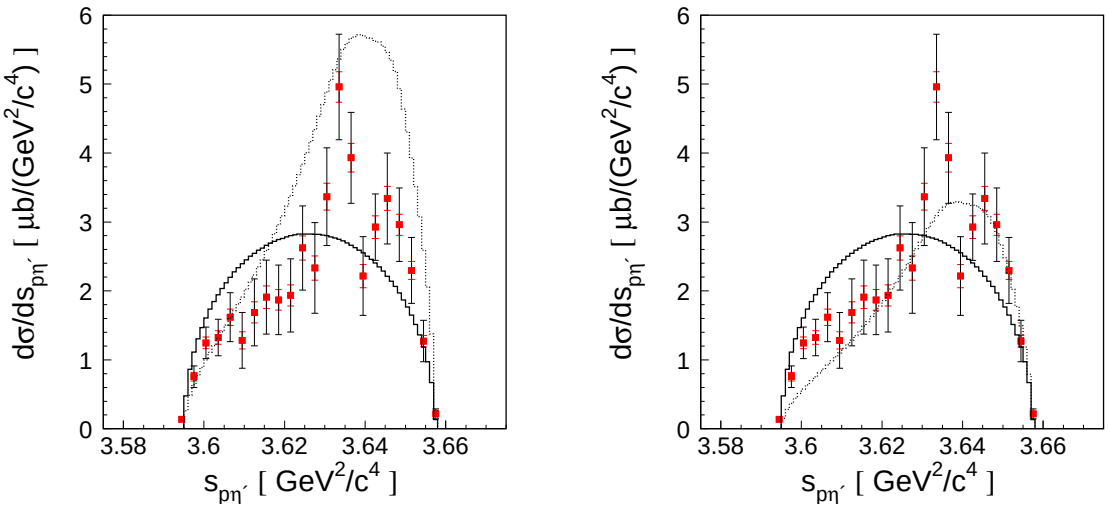

Figure 10.14: Distribution of the square of the proton-η' ($s_{p\eta'}$) invariant mass determined experimentally for the $pp \to pp\eta'$ reaction (closed squares). The integrals of the phase space weighted by a square of the proton-proton on-shell scattering amplitude (dotted lines)-FSI$_{pp}$ normalized arbitrarily to the lower values of $s_{p\eta'}$ in the left panel and to the higher values of $s_{p\eta'}$ in the right panel. The expectations under the assumption of the homogeneously populated phase space are shown as solid lines.

Inspecting figures 10.13 and 10.14, one can conclude that similarly to the case of the $pp \to pp\eta$ reaction, the proton-proton on-shell interaction is not sufficient to explain the enhancement seen in both distributions, independent of the applied normalization.

A better description is obtained when instead of the on-shell proton-proton amplitude the proton-proton FSI is parameterized by the Jost function [1, 78].
The experimental distributions of s_{pp} and $s_{p\eta'}$ are compared to the theoretical model proposed by V. Baru and collaborators [39] in figure 10.15.
The model is based on calculations in which the overall transition matrix element can be factorized into the primary production and the proton-proton final state interaction expressed as the inverse of the Jost function derived from the Bonn potential [1, 39, 79]. The production amplitude is calculated using the one boson exchange model (OBE) and is nearly constant in the calculations. One can see that the model normalized to the total cross section, hardly fit to the experimental data at the range of lower and higher s_{pp} values. On the other hand, the $s_{p\eta'}$ distribution is rather well reproduced by the model.

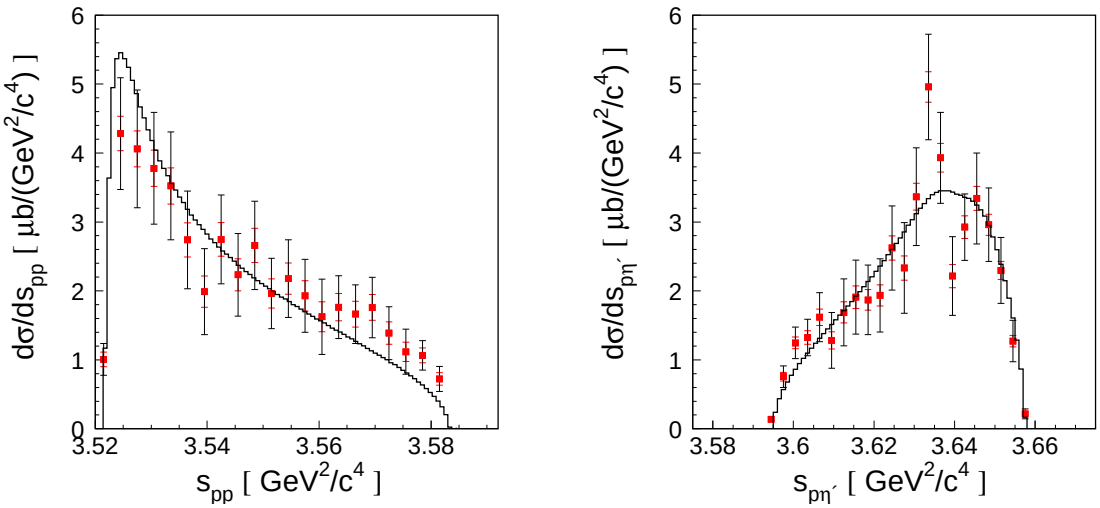

Figure 10.15: (Left) Distribution of the squared proton-proton (s_{pp}) invariant mass determined experimentally for the $pp \to pp\eta'$ reaction at the excess energy Q = 16.4 MeV (closed squares). (Right) Distribution of the squared proton-η' ($s_{p\eta'}$) invariant mass determined experimentally for the $pp \to pp\eta'$ reaction at the excess energy of 16.4 MeV (closed squares). The experimental data are compared to the calculations under the assumption of the ${}^3P_0 \to {}^1S_0 s$ transition according to the model of V. Baru et al., as described in text and in [39, 79].

A better agreement with the experimental data can be achieved by the implementation of contributions from the higher partial waves in the theoretical calculations. In figure 10.16 the distributions of the squared masses of proton-proton (s_{pp}) and proton-η' ($s_{p\eta'}$) subsystems are compared to the calculations of K. Nakayama et al. [12].
The calculations result from a combined analysis (based on the effective Lagrangian approach) of the production of η and η' mesons in photo- and hadro-induced reactions[2] [12, 34, 80, 81]. The authors assumed in the calculations that the ${}^1S_0 \to {}^3P_0 s$ transition contributes beside the ${}^3P_0 \to {}^1S_0 s$ transition at the excess energy of 16.4 MeV.
Interestingly, the authors claim that for the $pp \to pp\eta'$ reaction the dominant production mechanism for the $NN \to NN\eta'$ reaction is due to the excitation of the intermediate S_{11} resonance [34]. Figure 10.16 shows that both distributions are well reproduced by the theoretical calculations.

[2]The general overview of the calculations proposed by K. Nakayama and group is discussed in appendix C.

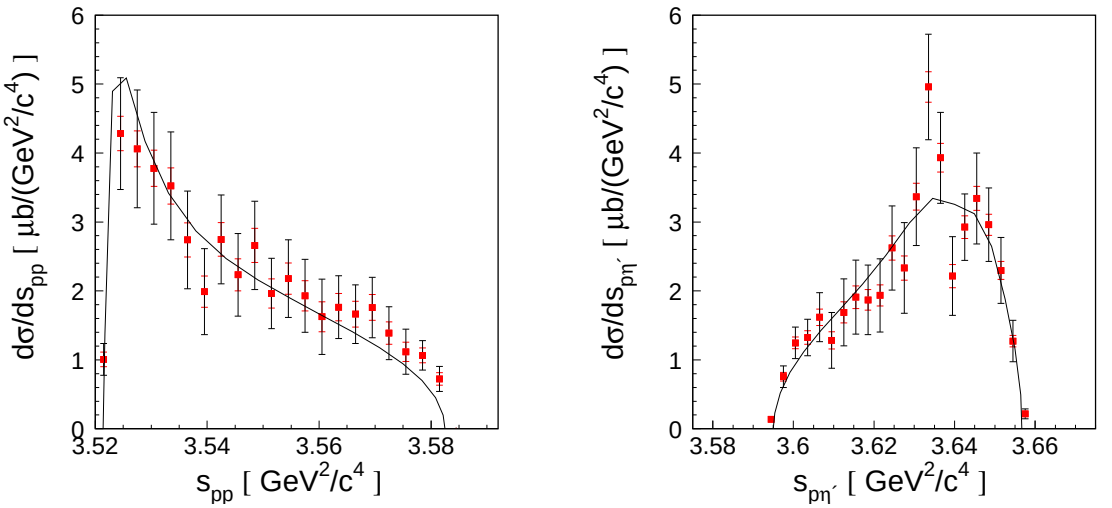

Figure 10.16: (Left) Distribution of the squared proton-proton (s_{pp}) invariant mass determined experimentally for the $pp \to pp\eta'$ reaction at the excess energy Q = 16.4 MeV (closed squares). (Right) Distribution of the squared proton-η' ($s_{p\eta'}$) invariant mass determined experimentally for the $pp \to pp\eta'$ reaction at the excess energy of 16.4 MeV (closed squares). The experimental distributions are compared to the calculations based on the assumption that S and P partial waves can contribute as it is described by K. Nakayama et al. in [12, 34, 80, 81].

On the other hand, as proposed by A. Deloff, one can explain the enhancement seen in the distributions by an energy dependent production amplitude, which in the calculations of V. Baru et al. [39, 79] and of K. Nakayama et al. [12, 34, 80, 81] was constant.
In figure 10.17 the experimentally determined spectra of the squared proton-proton invariant mass (s_{pp}) and proton-η' ($s_{p\eta'}$) system is presented and compared to calculations by A. Deloff [13, 82]. The calculations are based on the assumption that the production amplitude changes linearly with energy[3]. The calculations based on the standard on-shell approximation were modified allowing the linear energy dependence of the ${}^3P_0 \to {}^1S_0 s$ partial wave amplitude. Other partial wave transitions were neglected in the model.

[3]The phenomenological model of the differential cross section parameterization assuming the linear energy dependence of the production amplitude is presented in general in appendix D.

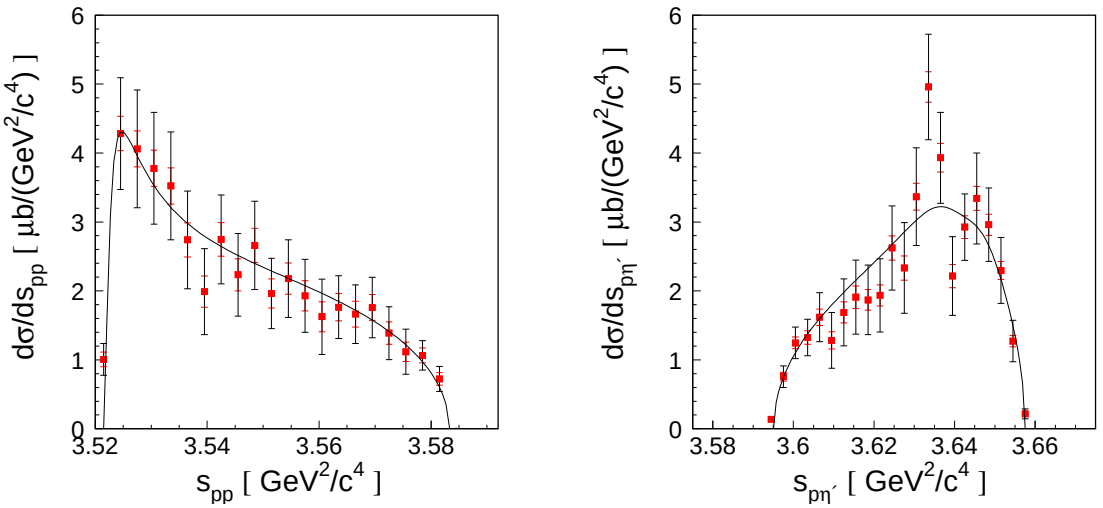

Figure 10.17: (Left) Distribution of the squared proton-proton (s_{pp}) invariant mass determined experimentally for the $pp \to pp\eta'$ reaction at the excess energy Q = 16.4 MeV (closed squares). (Right) Distribution of the squared proton-η' ($s_{p\eta'}$) invariant mass determined experimentally for the $pp \to pp\eta'$ reaction at the excess energy of 16.4 MeV (closed squares). The experimental data are compared to the calculations performed assuming a linear energy dependence of the production amplitude as proposed by A. Deloff [13, 82].

In conclusion to this chapter one has to stress that from the above presented considerations, the determined invariant mass distributions (s_{pp} and $s_{p\eta'}$) strongly deviate from the predictions based on the homogeneous population of events over the phase space. Also, the parameterization of the proton-proton on-shell interaction is not sufficient to explain the enhancement seen in the determined distributions.

Furthermore, one can see that both calculations assuming a significant contribution of P-wave in the final state (K. Nakayama), or the model assuming a linear energy dependence of the production amplitude by A. Deloff, reproduce the data within the error bars quite well. Therefore, on the basis of the presented invariant mass distributions, it is impossible to disentangle which of the discussed models is more appropriate.
On the other hand, it is clearly seen that the calculations assuming only ${}^3P_0 \to {}^1S_0 s$ transition, independent of the energy, underestimate the experimental data at the higher values and overestimate them at the lower values of s_{pp} as it is presented in figure 10.15.

Moreover, independently from the theoretical calculations, one can conclude from the comparison of s_{pp} and $\sqrt{s_{p-meson}}$ presented in figure 10.12 that the observed enhancement is not caused by a proton-meson interaction, since the strength of proton-η and proton-η' interaction is different but the enhancement in both cases is the same.

11. Summary

Differential distributions of the squared proton-proton (s_{pp}) and proton-η' ($s_{p\eta'}$) invariant masses, as well as angular distributions for the $pp \to pp\eta'$ reaction have been evaluated at an excess energy of Q = 16.4 MeV. The data were measured by the COSY-11 collaboration at the accelerator COSY.

The theoretical framework aiming to explain the unexpected enhancement observed in the invariant mass distributions determined for the $pp \to pp\eta$ reaction was presented and it was tried to verify one of the three challenging theories describing the observed behaviour by:

- a significant role of **proton-η interaction** in the final state,
- an **admixture of higher partial waves** in the produced proton-proton-meson system,
- an **energy dependence of the production amplitude**.

On a basis of only $pp \to pp\eta$ data, it was impossible to judge which model could describe the effects. Therefore, in order to verify those hypotheses by a comparison of the invariant mass spectra for the production of two different mesons, the analysis of the $pp \to pp\eta'$ reaction, presented in detail in this thesis, was performed.
The reaction was measured using the COSY-11 detector setup designed especially for close to threshold measurements. The experiment was performed at a beam momentum of $P_B = 3.260$ GeV/c, which corresponds to an excess energy of Q = 16.4 MeV.
A short description of the synchrotron COSY together with a closer look at the detectors of the COSY-11 apparatus used for the measurement was presented and its calibration and adjustment was described at length.
In the analysed experiment two charged particles were registered. Their identification as protons was based on the independent evaluation of their velocities and momenta. The decay products of the η' meson were not measured, therefore the number of $pp \to pp\eta'$ events was determined using the missing mass technique.

For the first time ever high statistics invariant mass s_{pp} and $s_{p\eta'}$ spectra and angular distributions, determined in the close to kinematical threshold region for the $pp \to pp\eta'$ reaction were presented. The distributions were corrected for the geometrical acceptance of the COSY-11 apparatus and were determined free from the background of the multi-pion production. Besides the differential distributions also the total cross section for the $pp \to pp\eta'$ reaction has been established, determined at an excess energy of Q = 16.4 MeV to be: $\sigma = (\mathbf{139} \pm \mathbf{3} \pm \mathbf{12})$ **nb**.

The evaluated invariant mass distributions were **similar to those determined for the η meson production. This result together with the shape of the excitation functions for the $pp \to pp\eta$ and $pp \to pp\eta'$ reactions, excludes the hypothesis postulating that the observed enhancement is caused by the interaction between proton and meson.**
Furthermore, the determined s_{pp} and $s_{p\eta'}$ differential distributions do not allow to judge between the proposed theoretical models. **Both, the hypothesis that an admixture of higher partial waves in the produced proton-proton-meson system and the proposal that an energy dependence of the production amplitude leads to the observed shape of the s_{pp} and $s_{p\eta'}$ distributions are consistent with the data at the achieved level of accuracy.**

The results presented in this thesis may be useful for the verification of other recently published theoretical models applied for the proton-proton-meson interaction, for example the calculations proposed by S. Ceci et al. in [83, 84].

In order to disentangle the possible explanations for the observed differential distributions more experimental data are required. The data base could be extended by studying the excess energy dependence of the shape of the s_{pp} and $s_{p\eta'}$ distributions, as it was done for the $pp \to pp\eta$ reaction. Such studies would allow for a direct comparison of the differential distributions behaviour for the η' production with already determined quantities for the $pp \to pp\eta$ reaction, in a similar manner as described in this thesis.

A more sensitive test, whether higher partial waves are indeed important for the studied reactions, could be gained from polarization observables. Therefore, measurement of analysing powers and spin correlation coefficients would be desirable for a better understanding of the dynamics and interaction in the $pp\eta$ and $pp\eta'$ systems.

A. Pseudoscalar mesons

Mesons are bound states built from a quark q and an antiquark $\bar{q}'$ according to the Quantum Chromodynamics, abbreviated as QCD. The quarks q and $\bar{q}'$ can be of the same or a different flavour. Since quarks possess the spin 1/2, they can build a singlet state with the total spin $J = 0$ or triplet states with the total spin $J = 1$.

A positive parity is assigned to the quarks whereas a negative parity is assigned to the antiquarks. Using that convention for the bound state of $q\bar{q}'$ and denoting by L the orbital angular momentum of the system, the parity of the meson built out of the quark pairs is $P = (-1)^{L+1}$.

From the three lighter quarks u, d and s nine possible $q\bar{q}'$ combinations can be built. This allows to built a meson nonet according to the SU(3) frame including the octet and the singlet state:

$$3 \otimes \bar{3} = 8 \oplus 1. \tag{A.1}$$

The assumption that these $q\bar{q}'$ systems are the ground state combinations of the quark-antiquark pairs with the angular momentum $L = 0$ implies, that the parity P of the constructed mesons should be equal to $P = -1$. With that conditions ($L = 0$ and $P = -1$) mesons with the internal spin $J = 1$ are called vector mesons, whereas mesons with the internal spin $J = 0$ are called pseudoscalar mesons.
The ground states of the pseudoscalar meson nonet is presented in figure A.1.

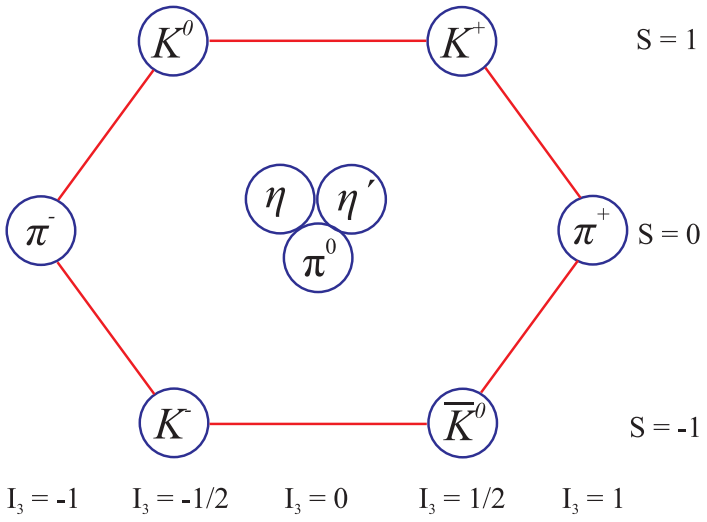

Figure A.1: The ground states of the pseudoscalar mesons ($J^P = 0^-$). The strangeness S of the mesons is plotted versus the third component of the isospin I_3.

The quark structure and masses of the ground states of the pseudoscalar mesons are listed in table A.1.

Pseudoscalar meson	Quark structure	Mass [MeV]
π^0	$1/\sqrt{2}(u\bar{u} - d\bar{d})$	134.98
π^+	$u\bar{d}$	139.57
π^-	$d\bar{u}$	139.57
K^+	$u\bar{s}$	493.68
K^-	$\bar{u}s$	493.68
K^0	$d\bar{s}$	497.61
$\bar{K}^0$	$\bar{d}s$	497.61
η	$A(d\bar{d} + u\bar{u}) + B(s\bar{s})$	547.85
η'	$a(d\bar{d} + u\bar{u}) + b(s\bar{s})$	957.66

Table A.1: List of the pseudoscalar mesons as the quark-antiquark combinations. Meson masses are taken from reference [5].

B. Parameterization of the proton-proton Final State Interaction

The total transition amplitude for the $pp \to ppX$ process can be written (in the Watson-Migdał approximation [85]) as [86]:

$$|M_{pp\to ppX}|^2 = |M_0|^2 \cdot |M_{FSI}|^2 \cdot ISI, \tag{B.1}$$

where M_0 denotes the total production amplitude, M_{FSI} refers to the elastic interaction among particles in the exit channel, and ISI stands for the reduction factor in the initial channel of the colliding protons.
The element $|M_{FSI}|$ is predominantly due to the pp-FSI ($M_{pp\to pp}$), which can be calculated as [87]:

$$M_{pp\to pp} = \frac{e^{\delta_{pp}(^1S_0)} \cdot sin\delta_{pp}(^1S_0)}{C \cdot k}, \tag{B.2}$$

where $C^2 = \frac{2\pi\eta_c}{e^{2\pi\eta_c}-1}$ is the Coulomb penetration factor [88], η_c is the relativistic Coulomb parameter.
The phase shift $\delta_{pp}(^1S_0)$ is calculated using the Cini-Fubini-Stanghellini formula with the Wong-Noyes Coulomb correction [18, 19, 89]:

$$C^2\ p\ ctg\delta_{pp} + 2p\ \eta_c\ h(\eta_c) = -\frac{1}{a_{pp}} + \frac{b_{pp}\ p^2}{2} - \frac{P_{pp}\ p^4}{1 + Q_{pp}\ p^2}, \tag{B.3}$$

where $h(\eta_c) = -ln(\eta_c) - 0.57721 + \eta_c^2 \sum_{n=1}^{\infty} \frac{1}{n(n^2+\eta_c^2)}$ [90],
$a_{pp} = -7.83$ fm,
and $b_{pp} = 2.8$ fm stand for scattering length and effective range, respectively [19].
The parameters $P_{pp} = 0.73$ fm^3, and $Q_{pp} = 3.35$ fm^2 are related to the shape of nuclear potential derived from one-pion-exchange model [19].

C. Formalism of a combined analysis of photo- and hadro-production of the η' meson

Investigations of the η and η' meson production are performed for the following reaction channels:

$$\gamma + N \rightarrow N + M,$$
$$\pi + N \rightarrow N + M,$$
$$N + N \rightarrow N + N + M, \tag{C.1}$$

based on a relativistic meson-exchange approach, where $M = \eta, \eta'$.
According to the model described in [91,92] the transition amplitude M [91]
for the $pp \rightarrow pp\eta'$ reaction is given by:

$$M = (1 + T_f G_f) J (1 + T_i G_i), \tag{C.2}$$

where $T_{i,f}$ denotes the NN T-matrix interaction in the initial (i) or final (f) state,
and $G_{i,f}$ is the corresponding two-nucleon propagator [91].
J sums all basic η' production mechanisms depicted in figure C.1.

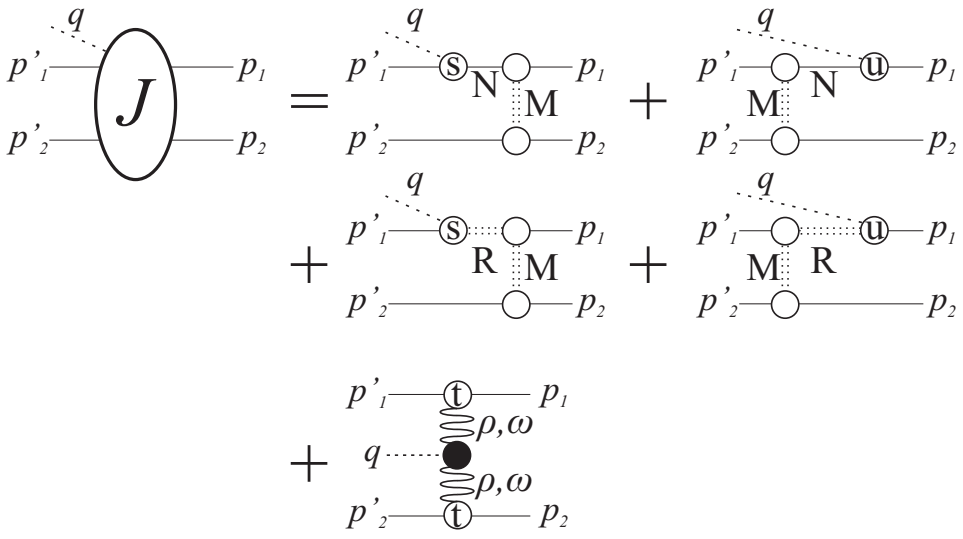

Figure C.1: Basic production mechanisms for the $pp \rightarrow pp\eta'$ reaction. Time proceeds from right to left for each individual graph. N and R denote the intermediate nucleons and resonances, respectively. M stands for all possible exchanges of mesons as: π, η, ρ, ω, σ and a_0 for the nucleon graphs (the first two graphs of the sum in figure C.1) and π, ρ and ω for resonance graphs (the third and the fourth graphs of the sum in figure C.1).

The free parameters of the model – i.e. resonance parameters and the NNM coupling constant – are fixed to reproduce the available data for photo- and hadron-induced reactions listed in equation C.1.

D. Linear energy dependence of the production amplitude

The following considerations and notation are adopted from reference [13].

The cross section for the $pp \to pp\eta'$ reaction can be expressed in the following manner:

$$\frac{d\sigma}{dLips} = |C(k)|^2[a + b\ P_2(\hat{p}\cdot\hat{q})] + C_0\ (\eta)[d\ ReC(k) + e\ ImC(k)]P_2(\hat{p}\cdot\hat{k}) \tag{D.1}$$

where in the standard notation *dLips* stands for the invariant three body phase space element, p denotes the initial momentum of the proton, k stands for the relative momentum of the two protons in the exit channel, and q corresponds to the relative momentum between meson and proton-proton pair in the final state. $C(k)$ and $C_0(\eta)$ denote enhancement factor and Coulomb penetration factor, respectively.
The a parameter denotes the modulus of the sole squared production amplitude which survives at threshold and is associated with the ${}^3P_0 \to {}^1S_0 s$ transition. The parameter b stands for the interference term between the latter amplitude and the ${}^3P_0 \to {}^2S_0 d$ amplitude. Parameters d and e correspond to the interference with a ${}^3P_2 \to {}^1D_2 s$ amplitude. The whole set of parameters depend on the final state momenta.

Looking at the threshold behaviour, one can see that the a parameter turns to be constant, the b parameter is proportional to q^2 and either d or e are of the order of k^2. In such a situation the a parameter has to be expanded to the same order by setting: $a = a_0 + a_1 q^2$ where a_0 and a_1 are two unknown parameters. The a_0 parameter can be absorbed in the normalization process and the ultimate expression for the cross section reads as:

$$\frac{d\sigma}{dLips} \propto |C(k)|^2\Big(1 + \frac{q^2}{q^2_{max}}[x + y\ P_2(\hat{p}\cdot\hat{q})]\Big) + \frac{k^2}{k^2_{max}} C_0(\eta)\Big[z_r\ ReC(k) + z_i\ ImC(k)\Big]P_2(\hat{p}\cdot\hat{k}) \tag{D.2}$$

where x, y, z_r and z_i are the dimensionless parameters to be determined. The x parameter stands for the correction of the order of q^2 to the dominant transition and the y, z_r and z_i parameters are the measure of the D-waves admixture.

Acknowledgments

First of all, this dissertation would have not come into life without enormous help of Prof. Paweł Moskal. I am really honoured and have a great pleasure to work with Him. I admire His knowledge and I would like to express my admiration for His patience, lots of fruitful ideas and great concepts.

I acknowledge Prof. Walter Oelert for being my supervisor during the stay in Jülich.

I am very grateful to Dr. Dieter Grzonka and Prof. Walter Oelert for all challenging ideas and help.

I thank Colleagues from the COSY-11 group for nice cooperation.

I would like to thank Dr. Rafał Czyżykiewicz for answers to all my questions. I really learnt a lot from Him.

Especially, I thank Marcin Zieliński for the whole bunch of expert's suggestions.

For careful reading and correcting this manuscript I am grateful to Prof. Walter Oelert, Dr. Dieter Grzonka and Prof. Paweł Moskal.

I acknowledge a big support of my family during the time of my studies.

Last but not least, I would like to thank my wife for being with me, sharing physics passion and daily life.

References

[1] P. Moskal, Habilitation Dissertation,
Jagiellonian University Press (2004), e-print arXiv:hep-ph/0408162.

[2] S. D. Bass, Acta Phys. Slov. **56** (2005) 245.

[3] S. D. Bass, Acta Phys. Pol. **B** Proc. Supl. 2 (2009) 11.

[4] S. D. Bass, A. W. Thomas, Phys. Lett. **B 634** (2006) 368.

[5] C. Amsler et al., Phys. Lett. **B 667** (2008) 1.

[6] C. P. Jessop et al., Phys. Rev. **D 58** (1998) 052002.

[7] G. Brandenburg et al., Phys. Rev. Lett. **75** (1995) 3804.

[8] K. Hagiwara et al., Phys. Rev. **D 66** (2002) 010001.

[9] P. Moskal et al., Phys. Rev. **C 69** (2004) 025203.

[10] A. Fix, H. Arenhövel, Phys. Rev. **C 69** (2004) 014001.

[11] A. Fix, H. Arenhövel, Nucl. Phys. **A 697** (2002) 277.

[12] K. Nakayama et al., Phys. Rev. **C 68** (2003) 045201.

[13] A. Deloff, Phys. Rev. **C 69** (2004) 035206.

[14] S. Brauksiepe et al., Nucl. Instr. & Meth. **A 376** (1996) 397.

[15] P. Klaja et al., AIP Conf. Proc. **796** (2005) 160.

[16] http://ikpe1101.ikp.kfa-juelich.de/

[17] R. Maier, Nucl. Instr. & Meth. **A 390** (1997) 1.

[18] H. P. Noyes, Ann. Rev. Nucl. Si. **22** (1972) 465.

[19] J. P. Naisse, Nucl. Phys. **A 278** (1977) 506.

[20] D. Sigg et al., Nucl. Phys. **A 609** (1996) 269.

[21] D. Sigg et al., Nucl. Phys. **A 617** (1997) 526.

[22] P. Moskal et al., Phys. Lett. **B 482** (2000) 356.

[23] F. Balestra et al., Phys. Lett. **B 491** (2000) 29.

[24] R. Wurzinger et al., Phys. Lett. **B 374** (1996) 283.

[25] P. Moskal et al., Phys. Rev. Lett. **80** (1998) 3202.

[26] P. Moskal et al., Phys. Lett. **B 474** (2000) 416.

[27] A. Khoukaz at al., Eur. Phys. J. **A 20** (2004) 345.

[28] F. Hibou et al., Phys. Lett. **B 438** (1998) 41.

[29] E. Chiavassa et al., Phys. Lett. **B 322** (1994) 270.

[30] H. Calén et al., Phys. Rev. Lett. **79** (1997) 2642.

[31] A. M. Bergdolt et al., Phys. Rev. **D 48** (1993) R2969.

[32] J. Smyrski et al., Phys. Lett. **B 474** (2000) 182.

[33] H. Calén et al., Phys. Lett. **B 366** (1996) 39.

[34] K. Nakayama, Y. Oh and H. Haberzettl Acta Phys. Pol. **B** Proc. Supl. 2 (2009) 23.

[35] R. Czyżykiewicz, private communication (2008).

[36] P. Klaja, R. Czyżykiewicz, P. Moskal, Acta Phys. Pol. **B** Proc. Supl. 2 (2009) 45.

[37] M. Abdel-Bary et al., Eur. Phys. J. **A 16** (2003) 127.

[38] H. Pettersson, Proceedings MENU 2007, Jülich, Germany, 10-14 Sep 2007, 276.

[39] V. Baru et al., Phys. Rev. **C 67** (2003) 024002.

[40] H.-H. Adam et al., Proposal for WASA-at-COSY, e-print arXiv: nucl-ex/0411038.

[41] http://wasasrv.ikp.kfa-juelich.de/WasaWiki/index.php/Main_Page

[42] http://www.fz-juelich.de/ikp/pisa/pisa.html

[43] http://www.iskp.uni-bonn.de/gruppen/edda/publ/top.html

[44] http://users.uj.edu.pl/ $\sim ufkamys/COSY13/$

[45] http://www.fz-juelich.de/ikp/anke/de/index.shtml

[46] http://www.fz-juelich.de/ikp/COSY-TOF/index_e.html

[47] http://www.fz-juelich.de/ikp/publications/AR2003/en/
vii_collaborations.shtml?jessica

[48] http://usparc.ihep.su/spires/find/experiments/www2?ee=COSY-NESSI

[49] http://www.fz-juelich.de/ikp/gem/gem.html

[50] http://www.iskp.uni-bonn.de/gruppen/momo/momo.html

[51] http://www.iskp.uni-bonn.de/gruppen/hires/index.html

[52] D. Prasuhn et al., Nucl. Instr. & Meth. **A 441** (2000) 167.

[53] H. Stockhorst et al., IKP Annual Report (1997) 160.

[54] H. Stockhorst, Shriften des FZ-Jülich, Matter and Materials **11** (2002) 176.

[55] R. Czyżykiewicz, Diploma Thesis,
Jagiellonian University, Cracow (2002), IKP Jül-4017.

[56] P. Moskal. Annul Report IKP-KFA (1996) 35.

[57] J. Przerwa, Diploma Thesis,
Jagiellonian University, Cracow (2004), IKP Jül-4141, e-print arXiv: hep-ex/0408016.

[58] T. Rożek, Ph.D. Dissertation, University of Silesia (2005) IKP Jül-4184.

[59] R. Bilger et al., Nucl. Instr. & Meth. **A 457** (2001) 64.

[60] P. Moskal et al., J. Phys. **G 32** (2006) 629.

[61] P. Moskal, Shriften des FZ-Jülich, Matter and Materials **21** (2004) 249.

[62] H. Dombrowski et al., Nucl. Instr. & Meth. **A 386** (1997) 228.

[63] A. Khoukaz et al., Eur. Phys. J. **D 5** (1999) 275.

[64] B. Gugulski et al., Annul Report IKP-KFA(I)-1992-3.

[65] Bicron Corporation, Newburry, OH 44065, USA.

[66] G. Anton et al., Nucl. Instr. & Meth. **A 310** (1991) 631.

[67] P. Moskal, Ph.D. Dissertation, Jagiellonian University,
Cracow (1998) IKP, Jül-3685.

[68] T. Sefzick, Annual Report of IKP (2002) 14, Berichte des FZ-Jülich, Jül-4052.

[69] W. R. Leo, Techniques for Nuclear and Particle Physics Experiments,
Springer - Verlag Berlin Heidelberg, 1997.

[70] P. Moskal et al., Nucl. Instr. & Meth. **A 466** (2001) 448.

[71] M. Zieliński, Diploma Thesis,
Jagiellonian University, Cracow (2008), IKP Jül-4277, e-print arXiv: hep-ex/0807.0576.

[72] D. Albers et al., Phys. Rev. Lett. **78** (1997) 1652.

[73] K. Kilian, R. Maier, S. Martin, U. Pister, (1990),
Cooler synchrotron COSY Jülich - User Guide.

[74] D. Prasuhn, private communication (2006).

[75] H. Stockhorst, private communication (2006).

[76] F. Balestra et al., Phys. Rev. Lett. **89** (2002) 092001.

[77] J. Ritman, Habilitation Dissertation, Giessen University (2000).

[78] M. L. Goldberger and K. M. Watson, "Collision Theory", John Wiley & Sons,
New York (1964).

[79] V. Baru et al., Phys. Atom. Nucl. **64** (2001) 579.

[80] K. Nakayama, H. Haberzettl, Phys. Rev. **C 69** (2004) 065212.

[81] K. Nakayama, Y. Oh, H. Haberzettl, e-print: arXiv: hep-ph/0803.3169.

[82] A. Deloff, private communication (2009).

[83] S. Ceci, A. Švarc, B. Zauner, Acta Phys. Pol. **B** Proc. Supl. 2 (2009) 157.

[84] S. Ceci, A. Švarc and B. Zauner, Phys. Scripta **73** (2006) 663.

[85] K. M. Watson, Phys. Rev. **88** (1952) 1163.

[86] A. Moalem et al., Nucl. Phys. **A 589** (1995) 649.

[87] B. J. Morton et al., Phys. Rev. **169** (1968) 825.

[88] H. A. Bethe, Phys. Rev. **76** (1949) 38.

[89] H. P. Noyes, H. M. Lipinski, Phys. Rev. **C 4** (1971) 995.

[90] J. D. Jackson, J. M. Blatt, Rev. of Mod. Phys. **22** (1950) 77.

[91] K. Nakayama, J. Speth and T.-S. H. Lee, Phys. Rev. **C 65** (2002) 045210.

[92] K. Nakayama, H. F. Arellano, J. W. Durso and J. Speth,
Phys. Rev. **C 61** (1999) 024001.